# Influence of flow thickness on general relativistic low angular momentum accretion around spinning black holes

Pratik Tarafdar[†]

*S. N. Bose National Centre For Basic Sciences, Block-JD, Sector-III, Salt Lake, Kolkata 700106, India*

Susovan Maity[‡] and Tapas K. Das[*]

*Harish-Chandra Research Institute, HBNI, Chhatnag Road, Jhunsi, Allahabad 211109, India*

(Received 30 November 2020; accepted 7 January 2021; published 22 January 2021)

General relativistic, axisymmetric flow of low angular momentum accretion around a Kerr black hole can assume certain geometric configurations where the flow is maintained in hydrostatic equilibrium along the vertical direction (the direction orthogonal to the equatorial plane of the flow). The flow thickness for such accretion models becomes a function of the local radial distance measured from the black hole horizon. There are three types of functions defined in the literature which resemble the thickness of the flow for such a configuration. We formulate the equations governing the steady state astrophysical accretion characterized by both the polytropic as well as the isothermal equation of state in classical thermodynamics. We solve the equations within the framework of such geometric configuration for three different thickness functions to obtain the multitransonic, shocked, stationary integral accretion solutions. Such solutions enable us to study how flow thickness influences the dependence of the properties of postshock flows on black hole spin angular momentum, i.e., the Kerr parameter. For temperature-preserving standing shocks, we find that the postshock part of the disc can become luminous, and a considerable amount of gravitational energy carried by the accreting fluid gets liberated at the shock. We find which kind of thickness function produces the maximum liberated energy, making the disc most luminous.

DOI: 10.1103/PhysRevD.103.023023

## I. INTRODUCTION

Axially symmetric, low angular momentum accretion of hydrodynamic fluid onto astrophysical black holes may exhibit multitransonic features, and such multitransonic accretion flow is endowed with a stationary shock. Such low angular momentum, practically inviscid flow may be observed in realistic astrophysical systems like detached binaries fed by accretion from stellar winds ejected by OB-type stars [1,2], semidetached low-mass nonmagnetic binary systems [3] and supermassive black holes fed by accretion from weakly rotating central stellar clusters ([4,5] and references therein). For a standard Keplerian accretion flow, various physical processes like turbulence produce practically inviscid low angular momentum flow (see e.g., [6] and references therein). Several recent works on accretion onto our Galactic Center black hole indicates the presence of such flow as well [7–17].

The multitransonic features and the formation of the corresponding standing shock have been studied extensively by several authors in the last forty years. Such efforts were initiated for black hole accretion under the influence of the post-Newtonian, pseudo-Schwarzschild and pseudo-Kerr potentials [9,18–40]. Eventually, shocked multitransonic flows were studied for general relativistic accretion flows as well [41–63], where the work by Fukue [20,64] may be attributed to the first ever paper published in the field of study of multitransonic shocked accretion flow. Of late, such shocked flows have been studied for magnetohydrodynamic black hole accretion and relativistic flows in other space-times [65–70].

Geometrical configuration of axisymmetrically accreting fluid can assume three different forms, see e.g., Sec. 4 of [71], for detailed discussions on such configurations. Also see [31,59] and references therein. In the present work, we concentrate on axially symmetric flows under hydrostatic equilibrium in the vertical direction, where the gravitational force on the accreting fluid is balanced against the fluid pressure force. These commonly used disc models, however, possess certain limitations, and there are certain proposals available in the literature to calculate a more realistic expression for the disc thickness, e.g., [72–76]. We, nevertheless, stick to the disc structure maintained in hydrostatic equilibrium along vertical directions, since dealing with the aforementioned alternate disc models is

[*]Corresponding author.
tapas@hri.res.in
[†]pratikta16@gmail.com
[‡]susovanmaity@hri.res.in

 

mathematically very difficult, if not impossible, while obtaining the stationary integral flow solutions from the general relativistic Euler and the continuity equations through a noncomputational analytical approach.

The first ever detailed calculation of the flow structure for general relativistic accretion onto rotating black holes was obtained by Novikov and Thorne (hereafter NT). They provided a particular expression of the disc thickness for flow in hydrostatic equilibrium along the vertical direction [77].

Such an expression was slightly modified by Riffert and Herold (hereafter RH) [78] since the later work directly used the general relativistic Euler equation to derive the gravity-pressure balance equation, whereas in the first work the general relativistic version of the gravity-pressure balance equation was not directly derived. NT took the Newtonian gravity-pressure balance equation and replaced the vertical component of gravity-pressure balance with $R^z_{0z0}z$.

In recent years, Abramowicz, Lanza and Percival (hereafter ALP) [79] have provided a novel expression for disc thickness. In their calculations, ALP also derived the same gravity-pressure balance equation from the general relativistic equation. While simplifying the equation, they replaced the four-velocity component in such a way that no singularity in the disc height occurs at horizon. The main modification, apart from this careful choice of four-velocity, is that ALP used only one component of the relativistic Euler equation whereas RH did not assume trivial forms of four-velocities and solved two equations simultaneously for two components of the relativistic Euler equation.

In our present work, we will formulate and solve the general relativistic Euler and the continuity equations to observe how the aforementioned three different prescriptions for flow thickness influence the properties of the stationary integral flow solutions having more than one sonic transition and incorporating standing shock. Accretion flow governed by the polytropic as well as the isothermal equation of state will be studied.

We shall learn that for shock formation in isothermal flow, considerable amounts of energy may be released at the shock, which may enhance the brightness of the otherwise advection-dominated radiatively inefficient flow near the shock, and such a mechanism may explain the details of the flares emanating out of the black hole accretion disc as observed in various wavebands of the electromagnetic spectrum [80–83]. Our work, thus, sheds light on how a proposed flow thickness may contribute to understanding the variation of the disc luminosity during the generation of flares.

It is, however, to be understood that a complete description of the accreting black hole system requires the study of general relativistic magnetohydrodynamic flow under the influence of strong gravity. Such a system is difficult to study, even using large scale numerical simulations. Our humble approach, which involves a semianalytical study of the relativistic hydrodynamic flow of ideal fluid, attempts to capture certain essential features of the flares emanating out of our Galactic Center or from a similar setup where low angular momentum, practically inviscid accretion may be conceived. Our present work, thus, concentrates on the purely astrophysical aspects of the accretion phenomenon.

Nevertheless, our calculations may also find use in studying an accreting black hole system in a completely different context. It has been observed that a curved acoustic metric may be embedded within the accreting matter and such space-time may be generated through the perturbation of accretion flow [84–91]. The present work will also lead to the understanding of how the flow thickness of axially symmetric accretion in the Kerr metric may influence the properties of the analog surface gravity of the corresponding sonic space-time. It is, however, to be noted that analysis of such analog properties is beyond the scope of the present manuscript. Work is in progress along that direction and will be presented elsewhere [92].

Overall, the technical procedures followed to accomplish our goal are summarized below.

For three expressions of the flow thickness as classified in previous paragraphs, we shall formulate and solve the general relativistic Euler equation and the equation of continuity for relativistic ideal fluid, by assuming that the viscous transport of angular momentum may not play a significant role for low angular momentum advective accretion flow. We shall then solve such equations for the steady state flows and obtain stationary integral flow solutions which may make transitions from subsonic to supersonic state twice. We then introduce and discuss the mathematical conditions governing the formation of general relativistic standing shock, and solve such equations to obtain the shock location as a function of black hole spin angular momentum, i.e., the Kerr parameter. The properties of hotter, denser and shock-compressed postshock flow is then studied as the function of the Kerr parameter and the influence of the expression to the flow thickness on such properties is then realized.

## II. FLOW MODEL

### A. Background space-time

We represent the physical space-time of an uncharged, rotating black hole along its equatorial plane using the Kerr metric written in cylindrical Boyer-Lindquist coordinates [93]. The choice of coordinates is in accordance with cylindrical symmetry of the discs. Also for simplicity, we are interested in projection of the flow variables on the equatorial plane, obtained using vertical averaging technique as explained in subsequent sections. The line element for such a metric is given by

$$ds^2 = -\frac{r^2\Delta}{A}dt^2 + \frac{A}{r^2}(d\phi - \omega dt)^2 + \frac{r^2}{\Delta}dr^2 + dz^2, \quad (1)$$

where

$$\Delta = r^2 - 2r + a^2, \quad A = r^2 + r^2a^2 + 2ra^2, \quad \omega = \frac{2ar}{A}. \quad (2)$$

$\omega$ represents the rate of frame dragging by the black hole, $a$ being the Kerr parameter which in turn is related to the spin angular momentum $J$ of the black hole through the relation $a = J/M_{\rm BH}c$, where $-1 < a < 1$, $M_{\rm BH}$ is the mass of the respective black hole and $c$ is the velocity of light in vacuum. Calculations have been carried out using natural units, i.e., for $G = c = 1$, where $G$ is the universal gravitational constant. All masses are measured in units of $M_{\rm BH}$ which has been set to 1 for algebraic convenience, and can be easily substituted back using simple dimensional analysis. Distances are measured in units of $GM_{\rm BH}/c^2$, times are measured in units of $GM_{\rm BH}/c^3$ and all velocities are scaled in units of $c$. For a Kerr black hole, the horizon is located at the outer boundary of $g^{rr} = \Delta/r^2 = 0$, which is defined as $r_+$ and the expression of which is given by

$$r_+ = 1 + \sqrt{1 - a^2}. \quad (3)$$

### B. Choice of disc height

We consider the accretion disc around a Kerr black hole in hydrostatic equilibrium along vertical direction, i.e., the gravitational force component is balanced by the pressure of the fluid constituting the disc. The earliest general relativistic formulation of this gravity-pressure balance and thus a vertically averaged height prescription was proposed by Novikov and Thorne (NT) [77], and is given by

$$H_{\rm NT}(r) = \left(\frac{p}{\rho}\right)^{\frac{1}{2}} \frac{r^3 + a^2r + 2a^2}{r^{\frac{3}{2}} + a} \times \sqrt{\frac{r^6 - 3r^5 + 2ar^{\frac{9}{2}}}{(r^2 - 2r + a^2)(r^4 + 4a^2r^2 - 4a^2r + 3a^4)}}, \quad (4)$$

where $p$ and $\rho$ are pressure and rest-mass energy density of the fluid, respectively. It is to be noted that accretion flow described by the above disc thickness can not be extended up to $r_+$. The flow will be truncated at a *truncation radius* $r_T$, which is given by the solution of the equation

$$(r_T)^{\frac{1}{2}}(r_T - 3) = 2a, \quad (5)$$

and is greater than $r_+$. In reality, of course, the flow will exist up to $r_+$, but stationary integral flow solutions can not be formulated in the vicinity of $r_+$ for NT-type of discs, because the disc height cannot be defined for $r < r_T$.

The next prescription found in literature dealing with gravity-pressure balance and proposing a height recipe in the Kerr metric was by Riffert and Herold (RH) [78]. They modified the gravity-pressure balance condition of the treatment done in NT. Their proposed disc height is given by

$$H_{\rm RH}(r) = \left(\frac{p}{\rho}\right)^{\frac{1}{2}} \sqrt{\frac{r^5 - 3r^4 + 2ar^{\frac{7}{2}}}{r^2 - 4ar^{\frac{1}{2}} + 3ar^2}}. \quad (6)$$

Here also, the flow can only be extended inwardly up to $r_T$, which has the same value for NT, and for RH discs around the same black hole as given by Eq. (5).

Thus we see that both of the disc heights can be expressed in the form by $H(r) = (\frac{p}{\rho})^{\frac{1}{2}} f(r, a)$. The difference between these two models of disc thickness in vertical equilibrium is reflected by the difference in functional form of two different $f(r, a)$. The essential difference arises because whereas NT balanced the vertical component of pressure with a particular Riemann tensor $R^z_{0z0}$, which was equivalent to the vertical component of gravitational acceleration, RH derived the gravity-pressure balance equation by simultaneously solving two orthogonal projection components of the general relativistic Euler equation. We will observe that the Mach number evaluated at the critical points corresponding to the flow described by the thickness function proposed by NT will be identical with that of the flow described by the thickness functions proposed by RH. This is evident because the dynamical equation will have the same form in terms of $f(r, a)$, because the height prescription also has a similar form.

Abramowicz, Lanza and Percival (ALP) [79] introduced an expression for the disc thickness, given by

$$H_{\rm ALP}(r) = \left(\frac{p}{\rho}\right)^{\frac{1}{2}} \sqrt{\frac{2r^4}{v_\phi^2 - a^2(v_t - 1)}}. \quad (7)$$

Here, $v^\mu$ denotes the four-velocity of the fluid in an azimuthally-boosted frame that corotates with the flow. $v_\phi$ and $v_t$ are the azimuthal and temporal components of the covariant four-velocity, respectively, which are related by $\lambda = -v_\phi/v_t$, where $\lambda$ is the specific angular momentum of the flow and $v_t$ is given by [94]

$$v_t = \sqrt{\frac{\Delta}{B(1 - u^2)}}, \quad (8)$$

where $B = g_{\phi\phi} + 2\lambda g_{t\phi} - \lambda^2 g_{tt}$ and $u$ denotes advective velocity which is the three-component velocity in the corotating frame [95]. As mentioned earlier, no singularities in ALP-type disc heights occur at the horizon. Thus, ALP discs do not have any truncation constraints and the steady state accretion solutions can be obtained up to $r_+$.

## III. POLYTROPIC ACCRETION

### A. Fluid equations

#### 1. Fluid specification and sound speed

As specified earlier, we consider a low angular momentum accretion disc. The low angular momentum does not require the inward part of the disc to transfer momentum to the outside region through viscosity. Thus we consider a perfect fluid as the constituent of the accretion disc. The energy momentum tensor for a perfect fluid is given by

$$T^{\mu\nu} = (p+\epsilon)v^\mu v^\nu + pg^{\mu\nu}, \tag{9}$$

where $\epsilon$ is the total energy density of the fluid given by $\epsilon = \rho + \epsilon_{\text{thermal}}$, and where $\epsilon_{\text{thermal}}$ is the internal thermal energy density of the fluid.

The equation of state for adiabatic flow is given by $p = k\rho^\gamma$ where $\gamma$ is the adiabatic index and $k$ is a constant. Whereas for the isothermal case $p \propto \rho$, the sound speed for adiabatic flow (isoentropic flow) is given by

$$c_s^2 = \left.\frac{\partial p}{\partial \epsilon}\right|_{\text{entropy}} = \frac{\rho}{h}\frac{\partial h}{\partial \rho}, \tag{10}$$

where $h$ is the enthalpy given by

$$h = \frac{p+\varepsilon}{\rho}. \tag{11}$$

#### 2. Conservation of specific energy

The energy-momentum conservation equation can be written as

$$D_\mu T^{\mu\nu} = 0, \tag{12}$$

where $D_\mu$ is the covariant derivative operator with respect to $\mu$. Equation (12), in turn, can be written using the definition of sound speed as

$$(p+\epsilon)v^\mu D_\mu v^\nu + (v^\mu v^\nu + g^{\mu\nu})\partial_\mu p = 0. \tag{13}$$

Now the thermodynamic equation of motion is given by

$$T\partial_\mu s = \partial_\mu h - \frac{\partial_\mu p}{\rho}, \tag{14}$$

where $s$ is the specific entropy. In case of polytropic accretion, the right-hand side of Eq. (14) is zero and Eq. (13) can be rewritten using normalization of four-velocity, which yields

$$u^\nu[D_\nu(hu_\mu) - D_\mu(hu_\nu)] = 0. \tag{15}$$

Using the time component of the equation and the fact that the flow is stationary, the conserved quantity from the energy-momentum conservation equation in case of polytropic accretion turns out to be

$$\mathcal{E} = hv_t = \text{constant}. \tag{16}$$

Substituting for $v_t$ from Eq. (8) and $h$ from Eq. (11) we obtain

$$\mathcal{E} = \frac{\gamma-1}{\gamma-1-c_s^2}\sqrt{\frac{\Delta}{B(1-u^2)}}. \tag{17}$$

Taking logarithmic derivative of both sides of Eq. (17) gives the gradient of adiabatic sound speed as

$$\frac{dc_s}{dr} = -\frac{\gamma-1-c_s^2}{2c_s}\left[\frac{u}{1-u^2}\frac{du}{dr} + \frac{1}{2}\left(\frac{\Delta'}{\Delta} - \frac{B'}{B}\right)\right]. \tag{18}$$

#### 3. Conservation of mass

The mass conservation equation is given by

$$D_\mu(\rho v^\mu) = 0. \tag{19}$$

A vertical averaging is done for convenience by integrating the flow equations over the $z$ coordinate and the resultant equation is described by the flow variables defined on the equatorial plane ($z = 0$). Furthermore, integration is done over $\phi$ which gives a factor of $2\pi$ due to the axial symmetry of the flow. We apply such vertical averaging as prescribed in [77,94,96] to the continuity equation given by Eq. (19). The vertically averaged $z$-component of the four-velocity becomes $v^z \sim 0$. Thus for the stationary ($t$-independent) and axially symmetric ($\phi$-independent) flow, the continuity equation turns out to be

$$\frac{\partial}{\partial r}(4\pi H_\theta\sqrt{-g}\rho v^r) = 0. \tag{20}$$

$H_\theta$ arises due to the vertical averaging and is defined as the local angular scale of flow. One can relate the actual local flow thickness $H(r)$ to the angular scale of the flow $H_\theta$ as $H_\theta = H(r)/r$, where $r$ is the radial distance along the equatorial plane from the center of the disc. $g$ is the value of the determinant of the metric $g_{\mu\nu}$ on the equatorial plane, $g = \det(g_{\mu\nu})|_{z=0} = -r^4$. Equation (20) gives the mass accretion rate $\dot{M}$ as

$$\dot{M} = 4\pi\sqrt{-g}H_\theta\rho v^r = 4\pi H(r) r\rho v^r. \tag{21}$$

The $r$ component of the four-velocity, $v^r$ is related to $u$ by the transformation law as

$$v^r = \frac{u}{\sqrt{g_{rr}(1-u^2)}} = \frac{\sqrt{\Delta}u}{r\sqrt{1-u^2}}, \tag{22}$$

using $g_{rr} = r^2/\Delta$. $\dot{M}$ can be written as

$$\dot{M} = 4\pi H(r)\Delta^{1/2}\rho\frac{u}{\sqrt{1-u^2}} = \text{constant}. \tag{23}$$

For adiabatic flow, a new quantity $\dot{\Xi}$ is obtained from $\dot{M}$ by multiplying it with $(\gamma k)^{\frac{1}{\gamma-1}}$. $\dot{\Xi}$ is a measure of the entropy accretion rate and is typically called the entropy accretion rate. The concept of the entropy accretion rate is widely used in accretion astrophysics. The entropy accretion rate was first defined in the literature by Blaes [23]. Expressing $\rho$ in terms of $\gamma$, $k$ and $c_s$ gives

$$\dot{\Xi} = \left(\frac{(\gamma-1)c_s^2}{\gamma-1-c_s^2}\right)^{\frac{1}{\gamma-1}} 4\pi H(r)\Delta^{1/2}\frac{u}{\sqrt{1-u^2}} = \text{constant}. \tag{24}$$

To express the entropy density in terms of $u$, $c_s$ and $r$ only, the expression of height must be written in terms of $u$ and $c_s$ also. For this we first note that, for adiabatic equation of state, $p/\rho$ can be written as

$$\frac{p}{\rho} = \left(\frac{1}{\gamma}\right)\left(\frac{(\gamma-1)c_s^2}{\gamma-1-c_s^2}\right). \tag{25}$$

This factor is common to all of the height prescriptions. For convenience, we distinguish the height factors in two classes: one consisting of the NT and RH models, and the other with the ALP model as its member. The reason behind this classification is that whereas the models in the first category can be written in generally as $H(r) = (\frac{p}{\rho})^{\frac{1}{2}} f(r,a)$, the model in the other category cannot be written as such. Thus we proceed separately for these two categories and derive the desired velocity gradients.

*NT and RH-type of discs.*— For these two models, we can write $H(r)$ from Eq. (4) and Eq. (6) as

$$H(r) = \left(\frac{1}{\gamma}\right)^{1/2}\left(\frac{(\gamma-1)c_s^2}{\gamma-1-c_s^2}\right)^{1/2} f(r,a), \tag{26}$$

where for NT

$$f_{\rm NT}(r,a) = \frac{r^3+a^2r+2a^2}{r^{\frac{3}{2}}+a} \times\sqrt{\frac{r^6-3r^5+2ar^{\frac{9}{2}}}{(r^2-2r+a^2)(r^4+4a^2r^2-4a^2r+3a^4)}}, \tag{27}$$

and for RH

$$f_{\rm RH}(r) = \sqrt{\frac{r^5-3r^4+2ar^{\frac{7}{2}}}{r^2-4ar^{\frac{1}{2}}+3ar^2}}. \tag{28}$$

Using the expression of $H(r)$ for both these models, $\dot{\Xi}$ can be written as

$$\dot{\Xi} = \sqrt{\frac{1}{\gamma}}\left(\frac{(\gamma-1)c_s^2}{\gamma-1-c_s^2}\right)^{\frac{\gamma+1}{2(\gamma-1)}} 4\pi\Delta^{1/2}\frac{u}{\sqrt{1-u^2}} f(r,a). \tag{29}$$

Taking the logarithmic derivative of both sides of the above equation and substituting $dc_s/dr$ using Eq. (18) gives

$$\frac{du}{dr} = \frac{u(1-u^2)[\frac{2}{\gamma+1}c_s^2(\frac{\Delta'}{2\Delta}+\frac{f'}{f})+\frac{1}{2}(\frac{B'}{B}-\frac{\Delta'}{\Delta})]}{u^2-\frac{c_s^2}{(\frac{\gamma+1}{2})}} = \frac{N}{D}. \tag{30}$$

*ALP-type of discs.*— From Eq. (7) and using the relation $\lambda = -\frac{v_\phi}{v_t}$, we have

$$H(r) = H_{\rm ALP}(r) = \left(\frac{1}{\gamma}\right)^{1/2}\left(\frac{(\gamma-1)c_{s0}^2}{\gamma-1-c_{s0}^2}\right)^{1/2}\sqrt{\frac{2r^4}{\lambda^2v_t^2-a^2(v_t-1)}}. \tag{31}$$

Thus using this expression of $H(r)$, the entropy accretion rate ($\dot{\Xi}$) can be obtained as

$$\dot{\Xi} = \sqrt{\frac{1}{\gamma}}\left(\frac{(\gamma-1)c_s^2}{\gamma-1-c_s^2}\right)^{\frac{\gamma+1}{2(\gamma-1)}} 4\pi\Delta^{1/2}\frac{u}{\sqrt{1-u^2}} \times\sqrt{\frac{2r^4}{\lambda^2v_t^2-a^2(v_t-1)}}. \tag{32}$$

Taking the logarithmic derivative of Eq. (32), we obtain

$$\frac{(\gamma+1)}{(\gamma-1-c_s^2)c_s}\frac{dc_s}{dr} = \frac{Pv_t(2\lambda^2v_t-a^2)}{4F} - \frac{\Delta'}{2\Delta} - \frac{2}{r} - \frac{du}{dr}\frac{1}{u(1-u^2)} \times\left(1-\frac{u^2v_t(2\lambda^2v_t-a^2)}{2F}\right), \tag{33}$$

where $P = \frac{\Delta'}{\Delta} - \frac{B'}{B}$ and $F = \lambda^2v_t^2 - a^2(v_t-1)$. Solving for $\frac{dc_s}{dr}$ from Eq. (33) and equating with Eq. (18), we yield

$$\frac{du}{dr} = \frac{\frac{2c_s^2}{\gamma+1}(-\frac{Pv_t(2\lambda^2v_t-a^2)}{4F}+\frac{\Delta'}{2\Delta}+\frac{2}{r})-\frac{P}{2}}{\frac{u}{1-u^2}-\frac{2c_s^2}{\gamma+1}\frac{1}{(1-u^2)u}(1-\frac{u^2v_t(2\lambda^2v_t-a^2)}{2F})} = \frac{N}{D}. \tag{34}$$

### B. Critical point conditions

In this section, we will present the scheme and calculations for finding the stationary transonic flow solutions for all three flow thicknesses considered in this work. We present NT and RH discs in the first category and ALP discs in the second category for reasons stated earlier.

### 1. NT and RH-type of discs

Borrowing a standard procedure from dynamical systems theory [97–99], we set the numerator and denominator of $du/dr$ to zero separately in order to obtain the necessary conditions to be satisfied at the critical points of the system. Setting $D = 0$ we get

$$u^2|_c = c_s^2|_c / \left(\frac{\gamma+1}{2}\right), \tag{35}$$

where the suffix $c$ denotes its value evaluated at the critical point. By setting $N = 0$, we yield

$$c_s^2|_c = \left(\frac{\gamma+1}{4}\right) \frac{\frac{B'}{B} - \frac{\Delta'}{\Delta}}{\left(\frac{\Delta'}{2\Delta} + \frac{f'}{f}\right)}. \tag{36}$$

In order to solve for the critical points, the critical point condition (35) is used in (17), which gives

$$\mathcal{E} = \frac{\gamma-1}{\gamma-1-(c_s^2)_c} \sqrt{\frac{(\gamma+1)\Delta_c}{B_c(\gamma+1-2(c_s^2)_c)}}, \tag{37}$$

where $(c_s^2)_c$ is a function of $r$ (evaluated at the critical point $r_c$) and the Kerr parameter $a$ obtained from (36). The solutions of this equation for a given set of system parameters $[\mathcal{E}, \lambda, \gamma, a]$ provide the critical points. The number of such critical points may be more than one, depending on the parameter values.

The value of $\frac{du}{dr}$ at the critical point is obtained by using l'Hôspital's rule in (30) as both the numerator and denominator tends to zero at the critical point. One obtains a quadratic equation for $(\frac{du}{dr})_c$ of the form

$$\alpha_1 \left(\frac{du}{dr}\right)_c^2 - \alpha_2 \left(\frac{du}{dr}\right)_c - \alpha_3 = 0, \tag{38}$$

where

$$\alpha_1 = 2(u)_c \left[1 - \frac{((c_s^2)_c - \gamma - 1)}{(\gamma+1)(1-(u^2)_c)}\right], \tag{39}$$

$$\alpha_2 = \frac{((c_s^2)_c - \gamma - 1)}{(\gamma+1)} \left(\frac{\Delta'}{\Delta} - \frac{B'}{B} + \left(\frac{\Delta'}{\Delta} + \frac{2f'_{\rm NT}}{f_{\rm NT}}\right)(u^2)_c\right) + \left[\frac{2}{\gamma+1}(c^2)_c \left(\frac{\Delta'}{2\Delta} + \frac{f'_{\rm NT}}{f_{\rm NT}}\right) + \frac{1}{2}\left(\frac{B'}{B} - \frac{\Delta'}{\Delta}\right)\right](1 - 3(u^2)_c), \tag{40}$$

$$\alpha_3 = (u)_c(1-(u^2)_c)\left[\frac{1}{2}\frac{\alpha'^2}{\alpha} - \frac{\alpha''}{2\alpha} + \frac{2(c_s^2)_c}{\gamma+1}\left(\frac{\Delta''}{2\Delta} + \frac{f''}{f} - \frac{1}{2}\frac{\Delta'^2}{\Delta} - \frac{f'^2}{f}\right) + \frac{((c_s^2)_c - \gamma - 1)}{(\gamma+1)}\left(\frac{\Delta'}{2\Delta} + \frac{f'}{f}\right)\left(\frac{\Delta'}{\Delta} - \frac{B'}{B}\right)\right]. \tag{41}$$

The two roots of the quadratic equation (38) signify two different slopes of two different integral solutions passing through each critical point, while such slopes are measured at the respective critical points only.

Once we are equipped with the values of the critical points and the critical gradients, the phase portrait (i.e., the $u$ vs $r$ diagram) can be plotted by numerically integrating the expression of $du/dr$ [Eq. (30)] for a particular set of $[\mathcal{E}, \lambda, \gamma, a]$, as will be illustrated in the subsequent sections. Here we substitute the value of $c_s^2$ from Eq. (24) as a function of parameters $\mathcal{E}$, $r$ and $u$. While addressing transonicity-related aspects of the flow, it is usually convenient to use the Mach number ($M = u/c_s$) instead of the advective flow velocity $u$.

### 2. ALP-type of discs

By setting $N = 0$ and $D = 0$, the critical conditions turn out to be

$$u^2|_{r_c} = \left.\frac{\rm P}{\frac{\Delta'}{\Delta} + \frac{4}{r}}\right|_{r_c}, \tag{42}$$

and

$$c_s^2|_{r_c} = \left.\frac{(\gamma+1)(2Fu^2)}{2(2F - u^2 v_t(2\lambda^2 v_t - a^2))}\right|_{r_c}. \tag{43}$$

To find the critical point we use the critical condition (43) in Eq. (17) and then solve the equation.

As observed from Eqs. (35), (42) and (43), the value of the Mach number at the critical point differs from unity for all three disc models considered in the present work. Hence the critical points do not coincide with the sonic points (by definition the sonic point is the location where the Mach number becomes unity). The value of the Mach number at critical points are found to be less than unity for all three types of disc thicknesses. For NT and RH kind of flow, the Mach number at the critical point is a constant $(\sqrt{\frac{2}{\gamma+1}})$ for a fixed value of $\gamma$. The departure of the value of the Mach number from unity has the same numerical value for all three critical points and hence three critical points lie on the same horizontal line parallel to the abscissa. For isothermal accretion, the value of the adiabatic index $\gamma$ will be one, and hence for isothermal flow the critical and the sonic points will be the same for NT as well as for RH-type of flow.

For ALP-type of disc, however, the amount of departure of Mach number (measured at the critical points) from unity is not constant. It rather depends on the value of the critical point itself, and thus on $[\mathcal{E}, \lambda, \gamma, a]$. Thus for ALP-type of disc, three different critical points for multicritical accretion will assume three different values of the Mach number, and three critical points will not lie of the same horizontal line for such a disc model. For ALP-type of disc, even for the isothermal flow, the Mach number does not become unity at the critical point.

Given a set of values of $[\mathcal{E}, \lambda, \gamma, a]$, one obtains the location of the critical point through the critical point analysis, and it is not required to integrate the fluid equations (the Euler equation or the equation of continuity). Among three critical points, the middle one is of center-type and hence no physical accretion solution can pass through it. Accretion solution can pass through the inner and the outer critical points only. Hence, one can have the sonic points corresponding to these two critical points, since both the innermost and the outermost critical points are of saddle-type. One thus computes the location of the critical point algebraically as discussed in Secs. III.B.1 and III.B.2, and then integrates the flow equations, starting from the critical point, up to the value of $r$ where the value of the Mach number becomes unity. That point is defined as the sonic point. We thus need to construct the integral accretion solution to find out the location of the sonic points corresponding to the inner-type and the outer-type critical points.

By following the same procedure as used to derive the slopes of trajectories through critical points, we find

$$\left.\frac{du}{dr}\right|_{r_c} = -\frac{\beta_{VE}}{2\alpha_{VE}} \pm \frac{1}{2\alpha_{VE}}\sqrt{\beta_{VE}^2 - 4\alpha_{VE}\Gamma_{VE}}, \quad (44)$$

where the coefficients $\alpha_{VE}$, $\beta_{VE}$ and $\Gamma_{VE}$ are given by $\alpha_{VE}=\frac{1+u^2}{(1-u^2)^2}-\frac{2nD_2D_6}{2n+1}$, $\beta_{VE}=\frac{2nD_2D_7}{2n+1}+\tau_4$, $\Gamma_{VE}=-\tau_3$, $n=\frac{1}{\gamma-1}$, $D_2=\frac{c_s^2}{u(1-u^2)}(1-D_3)$, $D_6=\frac{3u^2-1}{u(1-u^2)}-\frac{D_5}{1-D_3}-\frac{(1-nc_s^2)u}{nc_s^2(1-u^2)}$, $D_7=\frac{1-nc_s^2}{nc_s^2}\frac{P1}{2}+\frac{D_3D_4v_tP1}{2(1-D_3)}$, $\tau_3=\frac{2n}{2n+1}(c_s^2\tau_2-\frac{v_tP1v_1}{2nv_t}(1-nc_s^2)-c_s^2v_5v_t\frac{P1}{2})-\frac{P1'}{2}$, $\tau_4=\frac{2n}{2n+1}\frac{v_tu}{1-u^2}(\frac{v_1}{nv_t}(1-nc_s^2)+c_s^2v_5)$, $v_1=\frac{\Delta'}{2\Delta}+\frac{2}{r}-(2\lambda^2v_t-a^2)v_t\frac{P1}{4F}$, $D_3=\frac{u^2v_t(2\lambda^2v_t-a^2)}{2F}$, $D_4=\frac{1}{v_t}+\frac{2\lambda^2}{2\lambda^2v_t-a^2}-\frac{2\lambda^2v_t-a^2}{F}$, $D_5=D_3(\frac{2}{u}+\frac{D_4v_tu}{1-u^2})$, $\tau_2=\tau_1-\frac{v_t(2\lambda^2v_t-a^2)}{4F}P1'$, $v_5=(2\lambda^2v_t-a^2)\frac{P1}{4F}v_4$, $\tau_1=\frac{1}{2}(\frac{\Delta''}{\Delta}-\frac{(\Delta')^2}{\Delta^2})-\frac{2}{r^2}$, $v_4=\frac{v_3}{(2\lambda^2v_t-a^2)F}$, $v_3=(4\lambda^2v_t-a^2)F-(2\lambda^2v_t-a^2)^2v_t$.

### C. Parameter space

Having presented the complete scheme of drawing the phase portrait numerically, we focus our attention to the analysis of the parameter space of the system. $\mathcal{E}$ is scaled by rest-mass energy, which includes both rest-mass energy and thermal energy components. Setting $\mathcal{E}=1$ corresponds to an initial state where no thermal energy is present. Furthermore, setting $\mathcal{E}<1$ corresponds to initial conditions with negative energy. In this case, a dissipative mechanism is needed to extract energy from the flow so that a flow solution is obtained with positive energy. For our system of inviscid flow, this is not possible, and we consider flows with $\mathcal{E}>1$ only. All values of $\mathcal{E}$ greater than 2, although possible, correspond to extremely high initial thermal energy. Since this is not a common feature of accreting black hole systems, it is customary to restrict the system within the parameter range $1<\mathcal{E}<2$.

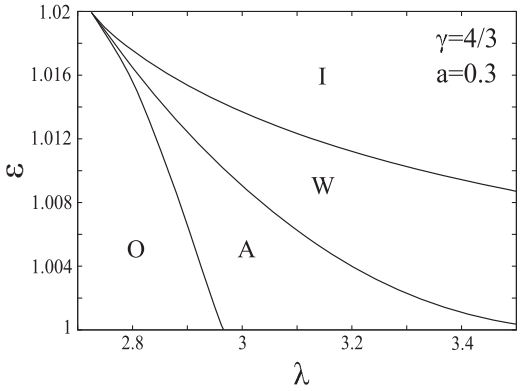


FIG. 1. $\mathcal{E}$ vs $\lambda$ plot for polytropic NT disc with $a=0.3$ and $\gamma=4/3$.

$\lambda=0$ implies a spherically symmetric flow, where $\lambda>4$ (in $G=M_{\rm BH}=c=1$ scaling) implies that the flow is not anymore in the Keplerian regime. In this region, multi-critical solutions do not generally occur. Thus we restrict ourselves to the parameter range of $0<\lambda<4$.

In isothermal fluids, adiabatic index $\gamma=1$. $\gamma>2$ corresponds to extremely dense fluids where comparatively large magnetic fields with direction dependence, i.e., anisotropic pressure are present. As we are not considering general relativistic magnetohydrodynamics, we should constrain ourselves in the domain $1<\gamma<2$. Moreover, throughout literature, the realistic limits to adiabatic index for accretion astrophysics is $\gamma=\frac{4}{3}$ for ultra-relativistic flows and $\gamma=\frac{5}{3}$ for nonrelativistic flows. Thus we will limit ourselves in the parametric range between $\frac{4}{3}<\gamma<\frac{5}{3}$.

Here we mention pro-grade flows, i.e., where the flow corotates with black hole and retrograde flows, i.e., where the flow counterrotates with the black hole. We consider both of these flows and in order to distinguish between the two we allow positive and negative values of $a$, whereas only positive values of $\lambda$ are allowed. Thus the range of $a$ is $-1<a<1$. An upper limit of 0.998 of $a$ has been set in some literature where interaction with the accretor and the accreting material has been considered [100]. In his work, Thorne considered the interaction of the accretion flow with the hole in such a way that the accretion flow can alter the mass and spin of the hole, which, however, we do not consider in our present work, since we are interested in non self-gravitating flow only. Thus, the present system of polytropic fluid accretion is studied within the parameter range $[1<\mathcal{E}<2, 0<\lambda<4, \frac{4}{3}<\gamma<\frac{5}{3}, -1<a<1]$.

Fig. 1 depicts the characteristic parameter space diagram for a polytropic NT disc. The NT disc has been selected for the purpose of demonstration because it is the oldest prescription of hydrostatic equilibrium models available in literature. All other prescriptions display the same general properties in this regard. For a fixed set of $[\gamma, a]$,

possible multicritical solutions form a wedge-shaped projection on the $\mathcal{E}-\lambda$ plane. The multicritical solutions constitute a set of three critical points, viz. $r_c^{\rm in}$, $r_c^{\rm mind}$ and $r_c^{\rm out}$, such that $r_c^{\rm in} < r_c^{\rm mind} < r_c^{\rm out}$. The region $A$ represents the "accretion solutions" for which the entropy accretion rate $\dot{\Xi}(r_c^{\rm in}) > \dot{\Xi}(r_c^{\rm in})$. The region $W$ consists of those solutions for which $\dot{\Xi}(r_c^{\rm in}) > \dot{\Xi}(r_c^{\rm in})$. Such solutions are known as "wind solutions". The curve dividing regions $A$ and $W$ covers those critical points through which *heteroclinic orbits* are formed in phase-space. Slight perturbations in the flow due to turbulence or other physical factors can push such solutions into either accretion or wind regime. Regions outside the wedge ($O$ and $I$) contain monocritical solutions. Inside region $O$, the critical point is of outer-type, which means it forms far away from the horizon, whereas inside region $I$, the critical points are formed nearer to the horizon and are known as inner-type. Both regions $O$ and $I$ contain single critical points (corresponding to monotransonic accretion/wind) up to a certain limit of flow parameters beyond which critical solutions cease to exist. However, since we are interested only in the $A$ region, a detailed discussion regarding the relation between system parameters and the existence or nonexistence of critical points lies beyond the scope of the present article.

### D. General relativistic polytropic shock conditions

Since we have assumed a nondissipative, inviscid flow, the specific energy and mass accretion rate are conserved. Thus, shocks formed in such flows must also preserve the conserved quantities. We consider the shock surface to be infinitesimally thin such that there are no temperature gradients within shock leading to any unwanted dissipation. Hence the discontinuity must satisfy the general relativistic Rankine-Hugoniot conditions [101–107] given below.

$$\begin{aligned} [\![\rho v^\mu \eta_\mu]\!] &= [\![\rho v^r]\!] = 0, \\ [\![T_{t\mu}\eta^\mu]\!] &= [\![(p+\varepsilon)v_t v^r]\!] = 0, \\ [\![T_{\mu\nu}\eta^\mu\eta^\nu]\!] &= [\![(p+\varepsilon)(v^r)^2 + p g^{rr}]\!] = 0, \end{aligned} \tag{45}$$

where $\eta_\mu = \delta^r_\mu$ is orthonormal to the surface of shock formation. For any arbitrary flow variable $f$, $[\![f]\!]$ is defined as $[\![f]\!] = f_+ - f_-$, where $f_+$ and $f_-$ are values of $f$ just outside and inside the shock, respectively. The difference measures the discontinuity in the flow variable due to shock. The first condition is conservation of mass accretion rate and the other two conditions are energy-momentum conservation. These conditions must be satisfied at the location where the shock forms. In order to find out the location of shock formation, a shock invariant quantity, which depends only on $u$, $c_s$ and $\gamma$, is constructed using the conditions above. The first and second conditions are trivially satisfied owing to the constancy of the mass accretion rate and the specific energy. The first condition is basically $(\dot{M})_+ = (\dot{M})_-$ and the third condition is $(T^{rr})_+ = (T^{rr})_-$. Thus a shock invariant quantity $S_{\rm sh}$ can be defined as

$$S_{\rm sh} = T^{rr}/\dot{M}, \tag{46}$$

which also satisfies $[\![S_{\rm sh}]\!] = 0$.

In order to calculate the shock invariant quantity we note that $h$ corresponds to the enthalpy of the stationary solutions of the steady state flow, given by Eq. (11). $c_s = (1/h)dp/d\rho = (1/h)k\gamma\rho^{\gamma-1}$, which gives $\rho$ (and hence also $p$ and $\epsilon$) in terms of $k$, $\gamma$ and $c_s$. Thus,

$$\begin{aligned} \rho &= k^{-\frac{1}{\gamma-1}}\left[\frac{(\gamma-1)c_s^2}{\gamma(\gamma-1-c_s^2)}\right]^{\frac{1}{\gamma-1}} \\ p &= k^{-\frac{1}{\gamma-1}}\left[\frac{(\gamma-1)c_s^2}{\gamma(\gamma-1-c_s^2)}\right]^{\frac{\gamma}{\gamma-1}} \\ \varepsilon &= k^{-\frac{1}{\gamma-1}}\left[\frac{(\gamma-1)c_s^2}{\gamma(\gamma-1-c_s^2)}\right]^{\frac{1}{\gamma-1}}\left(1+\frac{c_s^2}{\gamma(\gamma-1-c_s^2)}\right). \end{aligned} \tag{47}$$

Now $\dot{M} = \text{constant} \times rH(r)\rho v^r$ and $T^{rr} = (p+\varepsilon)(v^r)^2 + p g^{rr}$, where $v^r = u/\sqrt{g_{rr}(1-u^2)}$.

*NT & RH discs.*— The shock-invariant quantity $S_{\rm sh} = T^{rr}/\dot{M}$ becomes

$$S_{\rm sh} = \frac{(u^2(\gamma-c_s^2)+c_s^2)}{uc_s\sqrt{(1-u^2)(\gamma-1-c_s^2)}}, \tag{48}$$

where we have removed any overall factor of $r$ as shock invariant quantity is to be evaluated at $r = r_{\rm sh}$ for different branches of flow.

*ALP discs.*— In this case, the shock-invariant quantity turns out to be

$$S_{\rm sh} = \frac{(u^2(\gamma-c_s^2)+c_s^2)\sqrt{\lambda^2 v_t^2 - a^2(v_t-1)}}{uc_s\sqrt{(1-u^2)(\gamma-1-c_s^2)}}, \tag{49}$$

where $v_t$ is given in (8).

Fig. 2(a) shows edge-on view of the polytropic NT disc for flow with a given value of $[\mathcal{E}, \lambda, \gamma, a]$ in the presence of shock. Since specific energy is conserved in polytropic accretion, the postshock flow encounters a discontinuous increase in temperature, density and pressure. Consequently, the disc gets "puffed-up" at the shock location as is evident from the plot. A closer look at the central region of the disc [Fig. 2(b)] reveals that the disc gets terminated abruptly at the "truncation radius" ($r_T$) as defined in previous sections. It limits the use of such discs for analytically obtaining flow variables in close vicinity of the horizon (the quasi-terminal values) that are essential to constructing the image of the shadow of black holes [59]. Please refer to Sec. V for further discussions in this context. Figure 2(c) depicts a face-on view of one of the quadrants

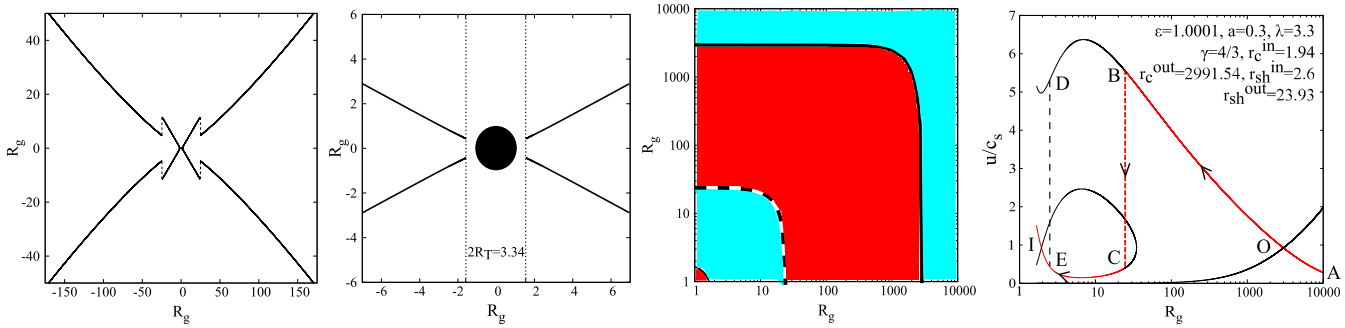


FIG. 2. (a) Disc height vs radial distance, (b) Central region in (a) is magnified, (c) Transonic boundaries–Cyan (lighter shade) region represents subsonic flow and red (darker shade) region represents supersonic flow, (c) Phase space trajectories–Mach number vs radial distance.

of the same disc on a logarithmic scale. The regions colored in cyan (lighter shade) and red (darker shade) represent regions of subsonic and supersonic flows, respectively. The solid boundary curves lie over points of continuous transonicity (transonic points corresponding to $r_c^{\rm out}$ and $r_c^{\rm in}$), while the dashed boundary curve lies over the points of discontinuous transonicity, i.e., shock. The flow profile becomes more explanatory in Fig. 2(d) where a complete phase-space diagram ($u/c_s$ vs $r$) for the given combination of flow parameters has been presented. Trajectory of the physical flow (marked in red) in the presence of shock has been indicated with arrows. The flow starts subsonically through the point $A$ and proceeds to cross the first transonic point $O$ (corresponding to the outer critical point $r_c^{\rm out}$) beyond which it attains supersonic velocities until point $B$. Here the flow encounters shock, causing a discrete jump onto point $C$ on the *homoclinic orbit*. The shock (dashed line $BC$) lies at the location $r_{\rm sh}^{\rm out}$, which can be calculated by looking for those values of $r$ where $S_{\rm sh}$ on the upper and lower branches become equal in magnitude. Using this procedure, a second shock location ($r_{\rm sh}^{\rm in}$, shown with the black dashed line $DE$) is sometimes obtained such that $r_{\rm sh}^{\rm in} < r_{\rm sh}^{\rm out}$. But such inner second shocks have been found to be unstable. In the absence of shock, the flow would have continued supersonically along the upper branch through $B$, effectively resulting in monotransonic accretion. However, transition onto $C$ brings the flow down to subsonic regime, and subsequently it follows the trajectory of the lower branch through the second transonic point $I$ (corresponding to the inner critical point $r_c^{\rm in}$) and proceeds beyond to fall into the horizon.

In Fig. 3, we plot the variation of the flow velocity $u$ [Fig. 3(a)], flow temperature $T$ [Fig. 3(b)], matter density $\rho$ [Fig. 3(c)] and the fluid pressure $P$ [Fig. 3(d)] as a function of the radial distance as measured from the horizon in terms of the Schwarzschild radius $R_g$ ($= 2GM_{\rm BH}/c^2$). In Figs. 3(a)–3(d), the variation is shown as a combination of two solid lines connected by a vertical dashed line. The solid line at the right of the dashed vertical line represents the variation along the flow solution passing through the outer sonic point (starting point of the solid line) and ending at the shock. The dashed vertical line corresponds to the discontinuous jump of the physical variable ($u$, $T$, etc.) at the shock location. The solid line to the left of the dashed vertical line represents the variation along the integral flow solution starting from the shock location and ending at the corresponding truncation radius for NT/RF discs given by Eq. (5). It is evident from the figure that the accretion flow slows down at the shock and gets compressed. Such relatively slow, shock-compressed postshock flow becomes

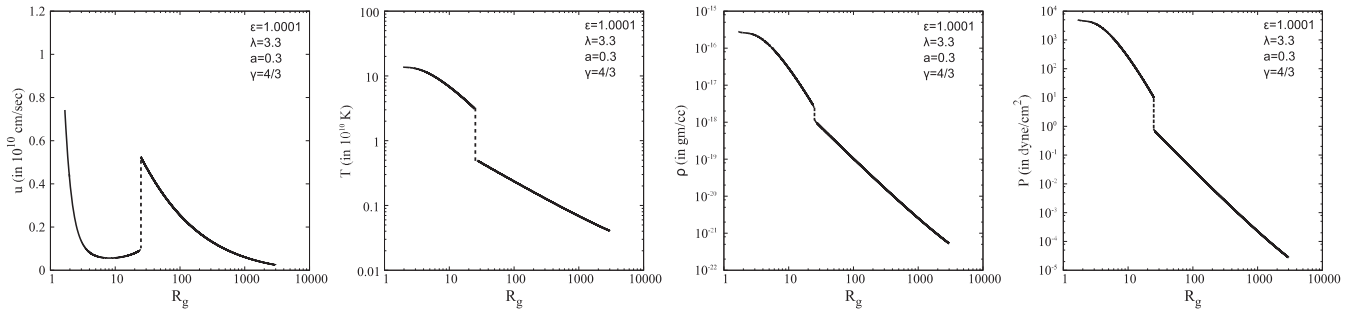


FIG. 3. Generic flow profiles–(a) Advective velocity ($u$) vs $R_g$, (b) Flow ion temperature ($T$) vs $R_g$, (c) Rest mass density ($\rho$) vs $R_g$, (d) Pressure ($P$) vs $R_g$. $u$ is in units of $10^{10}$ cm/ sec, $T$ is in units of $10^{10}$ Kelvin, $\rho$ is in units of gm/cc and $P$ is in units of dyn/cm$^2$.

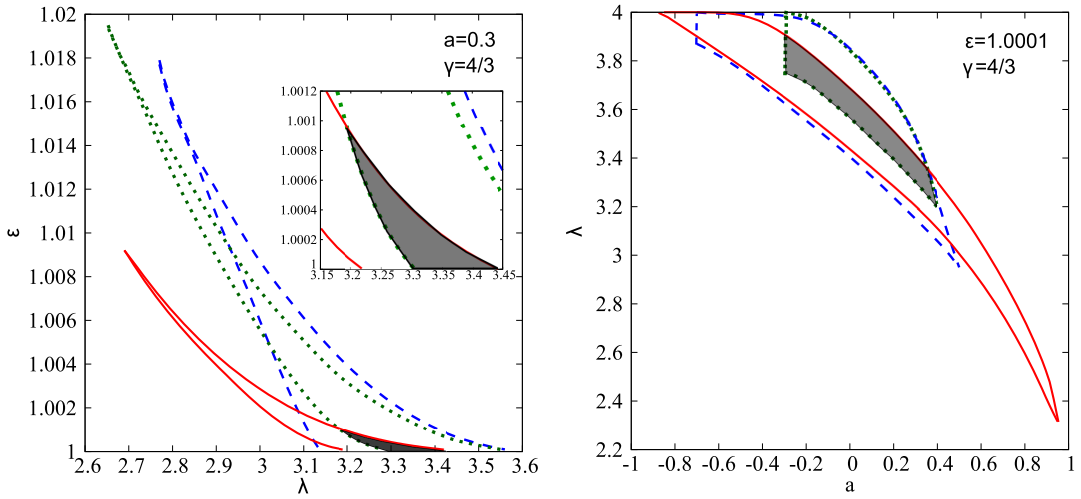


FIG. 4. Parameter space overlap for shocked solution–(a) $\mathcal{E}-\lambda$ plot and (b) $\lambda-a$ plot. Insets and shaded areas depict the common regions of shock solutions. ALP shown by red solid lines, RH shown by green dotted lines and NT shown by blue dashed lines.

hotter and denser. The energy-preserving hotter flow adiabatically expands and hence the postshock part of the disc gets puffed-up, as explained earlier.

As mentioned in the Introduction, our motivation is to compare various astrophysical properties of the shocked flow for three different disc thicknesses. We thus need to find out the region of the parameter space (parameters for which the shock forms) common to all such three different flow thicknesses.

In Fig. 4(a), we plot the $[\mathcal{E},\lambda]$ regions for which the shock forms for the flow having thickness as prescribed by NT (blue dashed curve in the online version of this article), RH (green dotted curve in the online version) and ALP (red solid curve in the online version). It is to be mentioned that from now onwards, the line types (solid, dotted and dashed) and the line colors (red, green and blue) corresponding to the three different disc models (ALP, RH and NT respectively) will be used in the same order (as used in the present diagram) throughout the paper, be it for polytropic or isothermal flow.

In Fig. 4(a), the overlap of the parameter spaces for the shock-forming flow corresponding to three different disc models is shown using a dark gray shade. The gray shaded common region has also been demonstrated in the inset of the figure. The figure has been drawn by keeping the values of the black hole spin and the adiabatic index of the flow to be fixed. The values of such fixed parameters are shown in the figure. Such values are representative values only, i.e., the shocked flow can be obtained for the other set of values of $[a,\gamma]$ as well.

Fig. 4(b) shows the parameter space diagram spanned by the flow angular momentum and the spin angular momentum of the black hole for a fixed set of values of $[\mathcal{E},\gamma]$ as specified in the figure. The set of values of $[\mathcal{E},\gamma]$ is representative and similar. $[\lambda,a]$ space can be obtained for other values of $[\mathcal{E},\gamma]$ as well. We choose the particular set of values $[\mathcal{E}=1.0001,\gamma=4/3]$ so that we can cover an extended range of the Kerr parameter to identify the shocked solutions. It is evident from the figure that the lower values of the black hole spin allow shock formation for relatively larger values of flow angular momentum, as well as for a relatively large span of values of the angular momentum. This is probably obvious because a lower spin accretor effectively reduces the influence of the flow angular momentum.

We conclude our discussions on parameter dependence of the shock solutions by studying the role of adiabatic index $\gamma$ and specific energy $\mathcal{E}$. Figure 5 depicts $[\gamma,a]$ space with shock solutions for different values of $\mathcal{E}$ and $\lambda$ corresponding to the ALP-type of discs. Similar panels can be constructed for NT and RH discs as well, but the trends of variation have been found to be similar. Due to the quality of not being constrained with any truncation radius and thus providing the maximum scope to look for shocks in terms of radial distance, the ALP disc has been chosen for the purpose of demonstration in this regard.

In Fig. 5(a), we see that the relevant adiabatic indices anticorrelate with the black hole spin parameter. Flows with four different values of specific energy ($\mathcal{E}_1>\mathcal{E}_2>\mathcal{E}_3>\mathcal{E}_4$, values provided in the respective figures and marked with blue, green, yellow and red colors, respectively) have been studied. We find that flows with lower values of $\mathcal{E}$ can lead to formation of shocks over a greater range of $\gamma$ from the fully relativistic limit of $\gamma=4/3$ until other intermediate values below the nonrelativistic limit of $\gamma=5/3$. The lowest value of $\mathcal{E}$ considered here ($\mathcal{E}_4=1.00001$) serves our purpose of explanation. However, even lower values of specific energy can be considered to predict shock solutions theoretically almost over the entire astrophysically relevant range of $\gamma$ (from fully relativistic to nonrelativistic flows). This, of course, comes with an obvious trade-off between the spans of results achieved and the computational costs incurred.

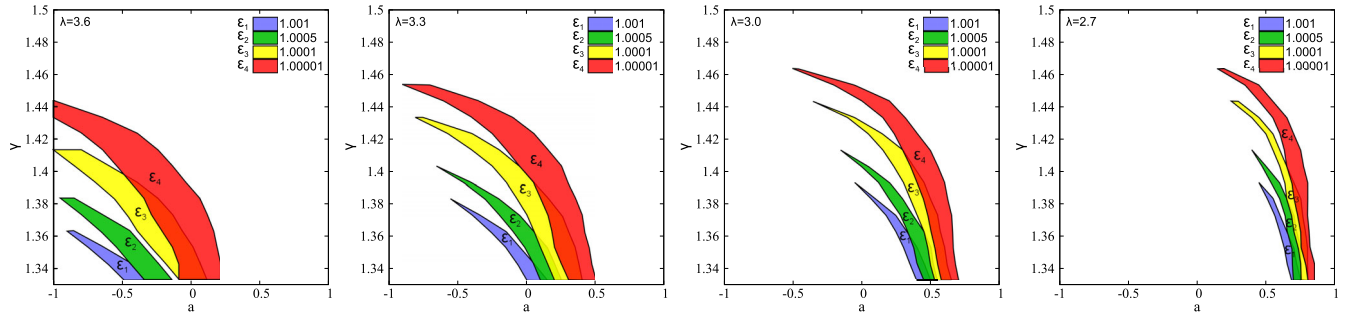


FIG. 5. $\gamma$-$a$ plot with different $\mathcal{E}$ values ($\mathcal{E}_1 = 1.001$, $\mathcal{E}_2 = 1.0005$, $\mathcal{E}_3 = 1.0001$, $\mathcal{E}_4 = 1.00001$) for (a) $\lambda = 3.6$, (b) $\lambda = 3.3$, (c) $\lambda = 3.0$ and (d) $\lambda = 2.7$.

Figs. 5(b)–5(d) show similar $\gamma$ vs $a$ plots depicting the shock-forming regions. The four separate figures (a)–(d) in the panel indicate the successively decreasing values of the flow angular momentum $\lambda$. We have already shown in Fig. 4(b) that the flow angular momentum and black hole spin anticorrelate with each other in the context of shock formation. Hence it is expected that as the value of $\lambda$ is decreased for a given set of $[\mathcal{E}, \gamma]$, shocks will be obtained at higher values of $a$. That is exactly what we see along Figs. 5(b)–5(d). However, it should also be noted that the range of $a$ over which such solutions are obtained decreases significantly with decreasing flow angular momentum. The interrelationships between all the system parameters are extremely complex for such highly nonlinear systems. A definitive picture can only be procured through generation of a complete four-dimensional parameter space diagram. Scanning the entire possible parameter space is heavily time-consuming and computationally exhausting, and hence is beyond our present theoretical scope. However, an integrated study of various parameter combinations as presented in our work provides a sufficiently comprehensive assessment of the relevant shock regimes.

In Fig. 6(a), we plot the shock locations (measured from the horizon in units of the Schwarzschild radius $R_g$ $[= 2GM_{\rm BH}/c^2]$), and other shock-related quantities as a function of the black hole spin for three different disc models. The set of values of $[\mathcal{E}, \lambda, \gamma]$ are kept fixed, and their fixed values are shown in the respective figures.

We observe that the shock location ($r_{\rm sh}$) correlates with the spin parameter of the black hole. This is intuitively obvious because higher spin effectively enhances the effect of flow angular momentum. The greater the angular momentum, the larger will be the distance at which the centrifugal barrier forms. The shock under consideration is centrifugal pressure supported. Hence, $r_{\rm sh}$ is pushed farther away from the horizon with increasing values of $a$. For fixed values of $[\mathcal{E}, \lambda, \gamma, a]$ the shock forms farthest for ALP-type of disc, whereas it forms closest for RH discs. For NT-type discs, the shock forms at an intermediate distance. $r_{\rm sh}$ vs $a$ curve for ALP-type discs approaches that for NT-type discs asymptotically but they never intersect. This has been investigated for values of $[\mathcal{E}, \lambda, \gamma, a]$ other than those used to generate Fig. 6. With decreasing $\lambda$, the overall set of $r_{\rm sh}$-$a$ curves shift towards higher values along the $a$ and $r_{\rm sh}$ axes. Thus, we find that $r_{\rm sh}$ anticorrelates with $\lambda$ as expected since $r_{\rm sh}$ correlates with $a$ and $a$ anticorrelates with $\lambda$. Similarly, the authors have verified that $r_{\rm sh}$ anticorrelates with $\gamma$ and correlates with $\mathcal{E}$ (since $\gamma$ anticorrelates and $\mathcal{E}$ correlates with $a$, as shown in Fig. 5).

At the shock location, directed flow velocity gets randomized and the gravitational potential energy available at the shock location determines the shock strength. The closer the shock forms to the horizon, the stronger it should be. Hence the strength should anticorrelate with the shock location and thus with the black hole spin parameter. This is exactly what we observe in Fig. 6(b). The shock strength is defined as the ratio of the pre- to postshock Mach number of the flow. We plot the shock strength ($M_-/M_+$, hereafter any accretion variable with a subscript "-" would indicate that it has been measured at the shock location before the shock is formed, i.e., it has been measured on the integral solution passing through the outer sonic point, and variables with subscript "+" would refer to the postshock values measured at the shock location on the integral solution passing through the inner sonic point) as a function of the Kerr parameter for both prograde and retrograde flow. As argued above, we clearly see that the shock strength anticorrelates with the black hole spin for both corotating as well as counterrotating flows. We observe an intersection of the $M_-/M_+$ vs $a$ curve for the ALP and NT disc models. Such intersection, by any means, does not indicate any degeneracy in the disc models, i.e., it does not mean that for certain values of $[\mathcal{E}, \lambda, \gamma, a]$ two or more separate disc models provide the same value of any significant accretion variable. It is important to note that the ratio of Mach numbers can assume same values at the point of intersection, but not the value of any individual quantity. The ratio of Mach numbers can be the same for two (or more) different sets of postshock values. The shock strength is found to correlate with $\lambda$ and $\gamma$, and anticorrelate with $\mathcal{E}$ as expected from the relation between the

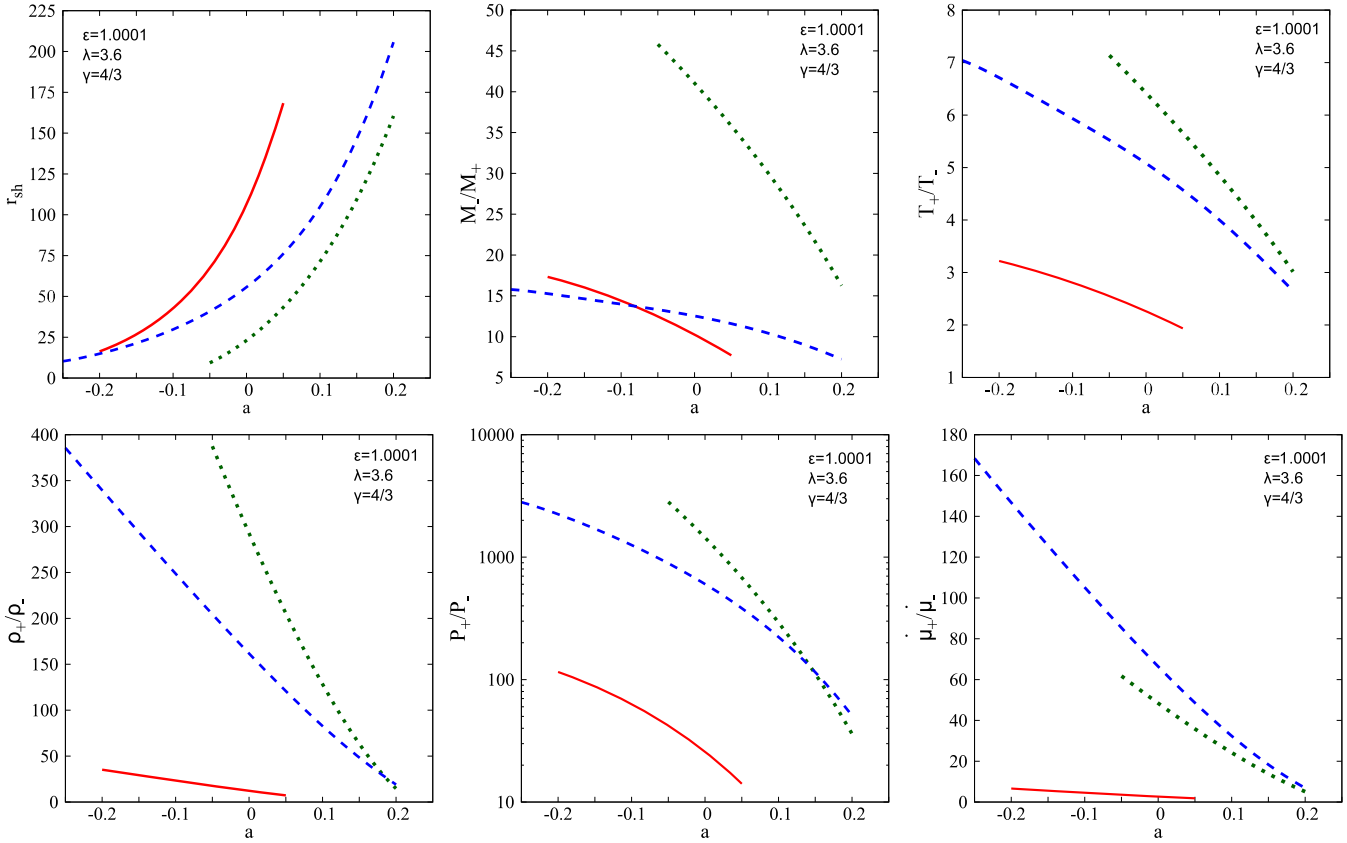


FIG. 6. Shock location–(a) $r_{\rm sh}$ (in terms of $R_g$) vs $a$, Ratios at shock–(b) $M_-/M_+$ vs $a$, (c) $T_+/T_-$ vs $a$, (d) $\rho_+/\rho_-$ vs $a$, (e) $P_+/P_-$ vs $a$ and (f) $\dot{\Xi}_+/\dot{\Xi}_-$ vs $a$. "−" and "+" refer to values "before" and "after" the shock respectively. ALP shown by red solid lines, RH shown by green dotted lines and NT shown by blue dashed lines.

corresponding parameters with $a$ shown previously in the respective parameter space diagrams. In Fig. 6(c) and 6(d), the post- to preshock temperature and shock compression ratio (ratio of flow densities after and before the shock) have been plotted against the change of black hole spin. As expected, these quantities anticorrelate with $a$ because the greater the amount of available gravitational potential energy at the shock, the higher the amount of temperature changes and the larger the amount of compression. It is evident from the figure that the RH-type of discs become most dense and hot after the shock forms whereas the ALP-type of discs change their temperature and density in minimum amounts at the shock. The NT kind of flow assumes an intermediate value for these two ratios. More or less, similar trends are observed for the variation of the ratio of the post- to the preshock fluid pressure for three different disc models. Here too, we find intersection among the two curves, but as explained earlier, it does not indicate any type of degeneracy. Finally, in Fig. 6(f) we plot the ratio of the post- to preshock entropy accretion rates for three disc models as a function of the black hole spin. The ratio of the entropy accretion rate is a measure of entropy production at the shock. As we observe, such a measure may not have any one-to-one correspondence with the shock strength. The entropy is directly related to the expression of the mass accretion rate of the steady-state flow.

In passing, we would like to mention that the set of $[\mathcal{E}, \lambda, \gamma]$ used to draw this figure is not unique by any means. We chose this set of values just to have a reasonable span of the black hole spin covering both prograde as well as retrograde flows. It is to be noted that shock does form for accreting black holes with intermediate as well as for higher values of spin, for both co- and counterrotating flows. One can obtain shocked flows for high-spin accretors using a suitable set of $[\mathcal{E}, \lambda, \gamma]$.

## IV. ISOTHERMAL ACCRETION

### A. Fluid equations

The equation of state characterising isothermal fluid flow is given by

$$p = c_s^2 \rho = \frac{\mathcal{R}}{\mu} \rho T = \frac{k_B \rho T}{\mu m_H}, \tag{50}$$

where $T$ is the bulk ion temperature, $\mathcal{R}$ is the universal gas constant, $k_B$ is Boltzmann constant, $m_H$ is mass of the hydrogen atom and $\mu$ is the mean molecular mass of fully

ionized hydrogen. The temperature $T$ as introduced in the above equation, and which has been used as one of the parameters to describe the isothermal accretion, is the temperature-equivalent of the bulk ion flow velocity. That is the reason why the value appears to be high ($10^{10}$–$10^{11}$ K) in this work. The actual disc temperature is the corresponding electron temperature, which should be of the of the order of $10^6$–$10^7$ Kelvin. Now using the equation of state (50), the equations needed to draw the phase portrait will be derived.

#### 1. Energy-momentum equation

Using Eq. (50), Eq. (13) can be rewritten as

$$u^\nu[D_\nu(\rho^{c_s^2}u_\mu) - D_\mu(\rho^{c_s^2}u_\nu)] = 0. \tag{51}$$

Using the time component of this equation and the stationary nature of the flow one obtains the conserved quantity

$$\xi = v_t\rho^{c_s^2}. \tag{52}$$

Taking the logarithmic derivative of Eq. (52), the derivative of density $\rho'$ is obtained as

$$\frac{\rho'}{\rho} = \frac{u'}{u(u^2-1)} - \left(\frac{f'}{f} + \frac{\Delta'}{2\Delta}\right). \tag{53}$$

#### 2. Continuity equation

In this section we again derive the velocity gradient for two separate classes, one consisting of NT and RH and the other consisting of the ALP height prescription. We note that we can still integrate continuity equation and the conserved quantity mass accretion rate $\dot{M}$ as defined in Eq. (23).

*For NT & RH discs.*—Using the fact that $\frac{p}{\rho}$ is the constant $c_s^2$, the height of the disc for these two height prescriptions in case of isothermal accretion can be written as

$$H(r) = c_s f(r,a). \tag{54}$$

Using Eq. (54) and putting the value of $\frac{\rho'}{\rho}$ in the logarithmic derivative of Eq. (23), we obtain

$$\frac{du}{dr} = \frac{u(1-u^2)[c_s^2(\frac{\Delta'}{2\Delta}+\frac{f'}{f}) + \frac{1}{2}(\frac{B'}{B}-\frac{\Delta'}{\Delta})]}{u^2-c_s^2} = \frac{N}{D}. \tag{55}$$

Again we mention that for NT height recipe, $f(r,a)$ is replaced by $f_{\rm NT}(r,a)$ as defined in Eq. (27) and for RH height recipe, we replace $f(r,a)$ by $f_{\rm RH}(r,a)$ as defined in Eq. (6).

*For ALP discs.*—For this recipe, the height function in the case of isothermal acretion is

$$H(r) = c_s^2\sqrt{\frac{2r^4}{\lambda^2 v_t^2 - a^2(v_t-1)}}. \tag{56}$$

Following the same procedure as used in previous class of height recipes, one yields

$$\frac{du}{dr} = \frac{c_{sc}^2(\frac{\Delta'}{2\Delta}+\frac{2}{r}-(2\lambda^2 v_t - a^2)\frac{v_t P}{4F}) - \frac{P}{2}}{\frac{u}{1-u^2} - \frac{c_{sc}^2}{u(1-u^2)}(1-(2\lambda^2 v_t - a^2)\frac{u^2 v_t}{2F})}, \tag{57}$$

where $P = \frac{\Delta'}{\Delta} - \frac{B'}{B}$ and $F = \lambda^2 v_t^2 - a^2(v_t-1)$.

### B. Critical point conditions

Following the same scheme as in polytropic process, we find the slopes of directrices at critical points, solve for the radial position of critical point $r_c$ and draw the phase portrait. Again we present NT- and RH-type of discs in the first class and ALP-type of discs in the next class for reasons stated earlier.

#### 1. For NT & RH discs

Setting $D = 0$ in Eq. (55) yields

$$u^2|_c = c_s^2|_c. \tag{58}$$

Setting $N = 0$ yields

$$c_s^2|_c = \frac{\frac{\Delta'}{\Delta}-\frac{B'}{B}}{(\frac{\Delta'}{2\Delta}+\frac{f'}{f})}. \tag{59}$$

To find the critical points for isothermal accretion the method followed is different from that of polytropic accretion as the basic parameter characterizing the flow is different for polytropic and isothermal accretion. In polytropic accretion, the parameters are $\mathcal{E}$ and $\lambda$, whereas the isothermal flow is characterized by the parameters $T$ and $\lambda$. So, by substituting the chosen value of the temperature $T$ in Eq. (50) we find the constant sound speed. Then, either the obtained value of $c_s^2$ is used in Eq. (59), or alternatively, the chosen value of $T$ is used in the following equation

$$\frac{\mathcal{R}}{\mu}T = \frac{\frac{\Delta'}{\Delta}-\frac{B'}{B}}{(\frac{\Delta'}{2\Delta}+\frac{f'}{f})}. \tag{60}$$

The right hand side of Eq. (60) is a function of the variable $r$ and by solving this equation the critical points are obtained.

The two values of the slopes at the critical point are obtained from the quadratic equation

$$\alpha_1\left(\frac{du}{dr}\right)^2 - \alpha_2\left(\frac{du}{dr}\right) - \alpha_3 = 0, \tag{61}$$

where

$$\alpha_1 = 4u_c, \tag{62}$$

$$\alpha_2 = \left(\frac{B'}{B} - \frac{\Delta'}{\Delta} + \left(\frac{\Delta'}{\Delta} + \frac{2f'}{f}\right)u_c^2\right)(1 - 3u_c^2), \tag{63}$$

$$\alpha_3 = u_c(1-u_c^2)\left[2u_c^2\left(\frac{\Delta''}{2\Delta} + \frac{f''}{f} - \frac{1}{2}\left(\frac{\Delta'}{\Delta}\right)^2 - \frac{f'^2}{f}\right) - \frac{\Delta''}{\Delta} + \frac{B''}{B} + \left(\frac{\Delta'}{\Delta}\right)^2 - \left(\frac{B'}{B}\right)^2\right]. \tag{64}$$

Thus we are equipped with all the information needed to draw the phase portrait diagram for a given parameter set of $[T, \lambda, a]$.

#### 2. For ALP discs

The critical point conditions obtained by setting $N = 0$ and $D = 0$ are

$$u_c^2|_{VE} = \frac{P1}{\frac{\Delta'}{\Delta} + \frac{4}{r}} \tag{65}$$

$$c_{sc}^2|_{VE} = \frac{u_c^2}{1 - \frac{u_c^2 v_t(2\lambda^2 v_t - a^2)}{2F}}. \tag{66}$$

Velocity gradient at critical points:

$$\left(\frac{du}{dr}\right)_c\Big|_{VE} = -\frac{\beta_{VE}}{2\alpha_{VE}} \pm \frac{1}{2\alpha_{VE}}\sqrt{\beta_{VE}^2 - 4\alpha_{VE}\Gamma_{VE}}, \tag{67}$$

where, $\alpha_{VE} = \frac{1+u_c^2}{(1-u_c^2)^2} - D_2 D_6$, $\beta_{VE} = D_2 D_7 + \tau_4$, $\Gamma_{VE} = -\tau_3$, $D_2 = \frac{c_s^2}{u(1-u^2)}(1 - D_3)$, $D_6 = \frac{3u^2-1}{u(1-u^2)} - \frac{D_5}{1-D_3}$, $D_7 = \frac{D_3 D_4 v_t P1}{2(1-D_3)}$, $\tau_3 = (c_s^2\tau_2 - c_s^2 v_5 v_t \frac{P1}{2}) - \frac{P1'}{2}$, $\tau_4 = \frac{c_s^2 v_5 v_t u}{1-u^2}$, $v_1 = \frac{\Delta'}{2\Delta} + \frac{2}{r} - (2\lambda^2 v_t - a^2)v_t \frac{P1}{4F}$, $D_3 = \frac{u^2 v_t(2\lambda^2 v_t - a^2)}{2F}$, $D_4 = \frac{1}{v_t} + \frac{2\lambda^2}{2\lambda^2 v_t - a^2} - \frac{2\lambda^2 v_t - a^2}{F}$, $D_5 = D_3(\frac{2}{u} + \frac{D_4 v_t u}{1-u^2})$, $\tau_2 = \tau_1 - \frac{v_t(2\lambda^2 v_t - a^2)}{4F}P1'$, $v_5 = (2\lambda^2 v_t - a^2)\frac{P1}{4F}v_4$, $\tau_1 = \frac{1}{2}(\frac{\Delta''}{\Delta} - \frac{(\Delta')^2}{\Delta^2}) - \frac{2}{r^2}$, $v_4 = \frac{v_3}{(2\lambda^2 v_t - a^2)F}$, $v_3 = (4\lambda^2 v_t - a^2)F - (2\lambda^2 v_t - a^2)^2 v_t$.

The location of critical points are solved just as described before; by putting appropriate $T$ in Eq. (50) and then solving Eq. (66) by using the corresponding value of $c_s$.

### C. The parameter space

In Fig. 7, we show that the parameter space spanned by the (constant) bulk flow temperature and the flow angular momentum for a particular value of the black hole spin ($a = 0.2$). Similar diagrams can be produced for other values of $a$, both for prograde as well as retrograde flows. As discussed in Sec. III. C, the parameter space is divided into four different regions, $O$, $I$, $A$ and $W$ as shown in the figure. The parameter space has been constructed for discs with NT-type of flow thickness.

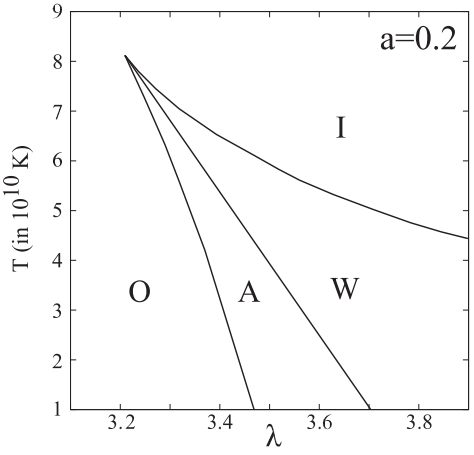


FIG. 7. $T - \lambda$ parameter space plot for accretion and wind in isothermal NT disc at $a = 0.2$.

Both regions $O$ and $I$ produce a single sonic (critical) point. For $O$, the sonic point is outertype, i.e., it forms far away from the horizon. Whereas for $I$, it is inner-type, i.e., it forms very close to the horizon. Parameter space region marked by $A$ designates accretion flow with three critical points. If shock forms, then the largest (outermost) and smallest (innermost) critical points may become sonic points and two different integral accretion solutions, passing through the outermost and the innermost critical (sonic) points respectively, may be joined using a stationary shock solution. For flow characterised by parameters chosen from region $A$, the quasi-specific energy measured along the integral accretion solution passing through the inner sonic point is less than the same measured along the solution passing through the outer sonic point ($\xi(r_c^{\rm in}) < \xi(r_c^{\rm out})$). The situation is just opposite for flows characterized by parameters taken from the region $W$. When parameters are taken from region $W$, the accretion flow can pass through only one sonic point, however the wind (outgoing) solutions can have three critical points. Outgoing solutions passing through the inner and the outer critical points may be joined through a stationary shock. We will, however, not discuss multitransonic shocked wind in the present work.

### D. General relativistic isothermal shock conditions

We note that $h = 1$ for isothermal process, which in turn yields

$$T^{rr} = \rho((v^r)^2 + c_s^2 g^{rr}). \tag{68}$$

#### 1. NT & RH discs

In this case the shock-invariant quantity turns out to be

$$S_{\rm sh} = \frac{(u^2(1-c_s^2) + c_s^2)}{u\sqrt{1-u^2}}, \tag{69}$$

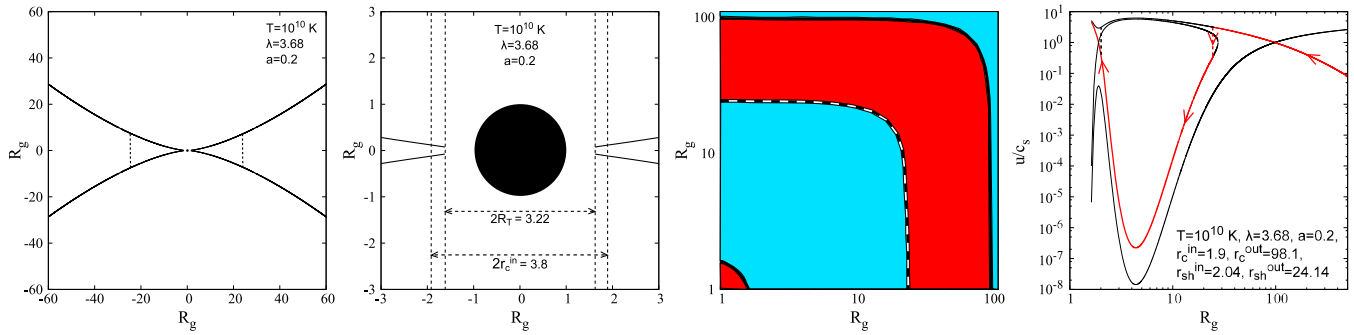


FIG. 8. Isothermal NT disc–(a) Disc height vs radial distance (in units of $R_g$) with vertical dotted lines depicting the shock locations ($r_{\rm sh} = 24.15$), (b) Magnified view of the central region depicting the truncation radius ($R_T$) and inner critical point ($r_c^{\rm in}$), (c) Face-on view of the disc (solid curves represent sonic points and dashed curve represents shock front. Regions shaded in cyan and red depict subsonic and supersonic flows respectively), (d) Mach number vs radial distance profile (red path depicts physical flow in the direction indicated with arrows).

where we have removed any overall factor of $r$ as shock invariant quantity is to be evaluated at $r = r_{\rm sh}$ for different branches of flow.

### 2. ALP discs

In this case, the shock-invariant quantity turns out to be

$$S_{\rm sh} = \frac{(u^2(1-c_s^2)+c_s^2)\sqrt{\lambda^2 v_t^2 - a^2(v_t-1)}}{u\sqrt{1-u^2}}, \qquad (70)$$

where $v_t$ is given in (8).

We show the multitransonic flow topology with shock for a set of $[T, \lambda, a]$ as specified in the diagram. We also show the segregated disc structure [the edge-on view in Fig. 8(a), and the face-on view in Fig. 8(c)] for various subsonic and supersonic parts of the flow, as clarified in much detail in Sec. III. D while describing features of Fig. 2. There is, however, a major difference between postshock disc structure in polytropic flow with energy-preserving shock and for isothermal flow with temperature-preserving shock. We have seen that for polytropic shocked accretion, lack of dissipation of energy increases the postshock flow temperature and the postshock part of the disc expands to produce a torus-kind of geometry. For isothermal shock, however, the thermal energy generated at the shock is allowed to liberate in order to maintain invariance of the flow temperature. Since no additional thermal energy gets trapped, the postshock disc, unlike its polytropic counterpart, does not get puffed-up. The energy liberated at the shock may power the strong flares emanating out of the axisymmetric accretion around supermassive black holes at the center of the galaxies. We shall elaborate this aspect in subsequent sections. In Fig. 8(b), the innermost part of the disc has been shown separately along with the termination radius ($R_T$) of the disc.

Fig. 9 shows the variation of the dynamical velocity $u$, the matter density $\rho$ and the fluid pressure $P$, as a function of the radial distance (measured from the horizon) for the shocked branch. The vertical dashed line signifies the discontinuous shock transition which joins the preshock flow solution passing through the outer sonic point with the postshock flow solution passing through the inner sonic point. For isothermal accretion, the sound speed remains invariant, hence the Mach number profile turns out to be just a scaled down version of the velocity profile.

Fig. 10(a) shows the parameter space (spanned by the flow temperature and flow angular momentum) for

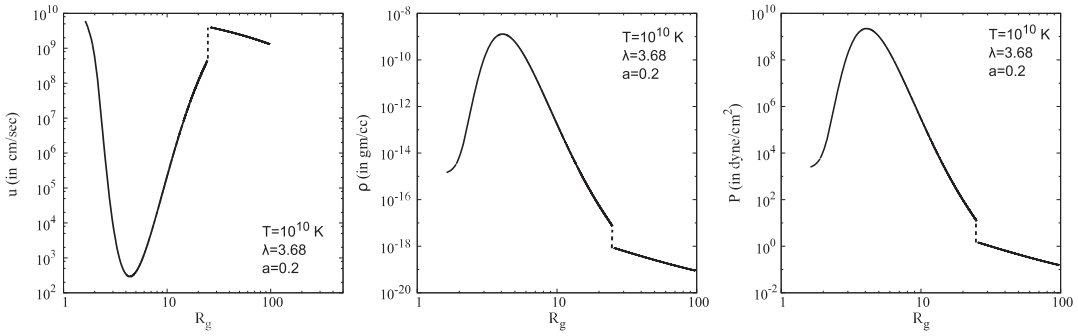


FIG. 9. Isothermal NT flow profile–(a) Advective flow velocity ($u$) vs $r$, (b) Rest mass density ($\rho$) vs $r$, (c) Pressure ($P$) vs $r$. $u$ in units of cm/ sec, $\rho$ in units of gm/cc, $P$ in units of dyn/cm$^2$ and $r$ in units of $R_g$.

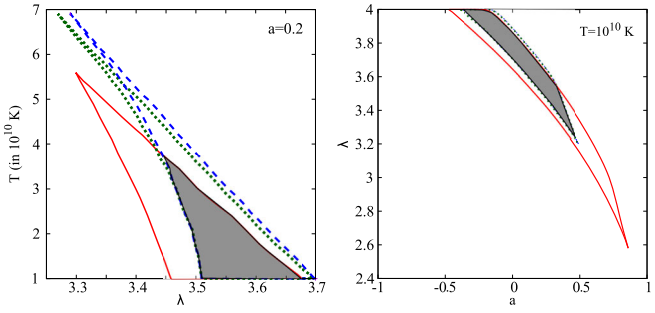


FIG. 10. Parameter space for shocked accretion flows–(a) Flow temperature ($T$) vs $\lambda$ ($a = 0.2$), (b) $\lambda$ vs $a$ ($T = 10^{10}$ K). Solid red curves, green dotted curves and blue dashed curves represent ALP, RH and NT discs respectively. Shaded regions depict overlap zones for the three disc models.

multitransonic shocked flow for three different disc thicknesses as considered in our work. The figure has been obtained for a fixed value of black hole spin $a = 0.2$. Similar figures can be obtained for any other value of $a$ for both prograde as well as retrograde flows. The region of parameter space common to all three disc thicknesses has been shaded in dark gray color.

The parameter space spanned by the flow angular momentum $\lambda$ and the black hole spin $a$ has been depicted in Fig. 10(b), for a fixed value of flow temperature $T = 10^{10}$ K. This value is only representative and similar diagrams with the same general features can be obtained for other values of $T$ as well. The particular value of $T$ has been chosen to cover an extended range of $a$ allowing shock solutions. Similar to the polytropic case [Fig. 4(b)], lower values of the Kerr parameter permit shock formation for flows with higher values of the specific angular momentum.

Fig. 11(a) shows the variation of shock location with the black hole spin for both the corotating as well as counterrotating flows. Faster rotating black holes produce the shock at larger distances for prograde flow whereas the trend is reverse in case of retrograde accretion. It should be noted that the NT- and RH-type discs produce shocks in extremely nearby locations for isothermal flows. Similar conclusions are drawn while observing the variation of the ratios of the pre-(post-) to the post-(pre-) shock accretion variables as a function of the Kerr parameter. Such variations are shown in Figs. 11(b)–11(d). The shock becomes stronger and the postshock flow becomes denser, as the shock location approaches towards the horizon. This is physically consistent as larger amounts of gravitational potential energy will be available for liberation when shock forms closer to the horizon. The results have been obtained for a particular set of $[T, \lambda]$. But results with the same variational trends can be obtained for any other relevant values of the given flow parameters.

### E. Energy dissipation at the temperature-preserving shock

The quasi-specific energy $\xi$ plays a role similar to that played by the entropy accretion rate $\dot{\Xi}$ for a polytropic flow. $\xi$ decreases after the flow encounters a shock. The difference of values of $\xi$ computed along the integral accretion solutions passing through the outer and the inner sonic points, respectively, is a measure of the flow energy liberated at shock. Such energy liberation mechanism may explain the formation and dynamics of flares (as observed in various wavelengths) emanating out from the proximity of our own Galactic Center black hole.

In Fig. 12, we plot the ratio of the pre- to postshock values of $\xi$ as a function of the Kerr parameter. As a reference, we also show the variation of corresponding shock locations with the black hole's spin. Three sets of figures have been produced for three different values of the flow angular momentum $\lambda$ and for the same value of the temperature as shown in the figure.

We expect that the ratio of $\xi$ at shock might anticorrelate with the shock location $r_{\rm sh}$, since for smaller values of $r_{\rm sh}$ (forming closer to the horizon, in a relatively stronger gravity regime), the gravitational potential energy available for liberation is higher. Also, values of the effective centrifugal barrier, i.e., $(\lambda \pm a)$, determine the amount of energy dissipated at the shock. For lower values of $(\lambda \pm a)$,

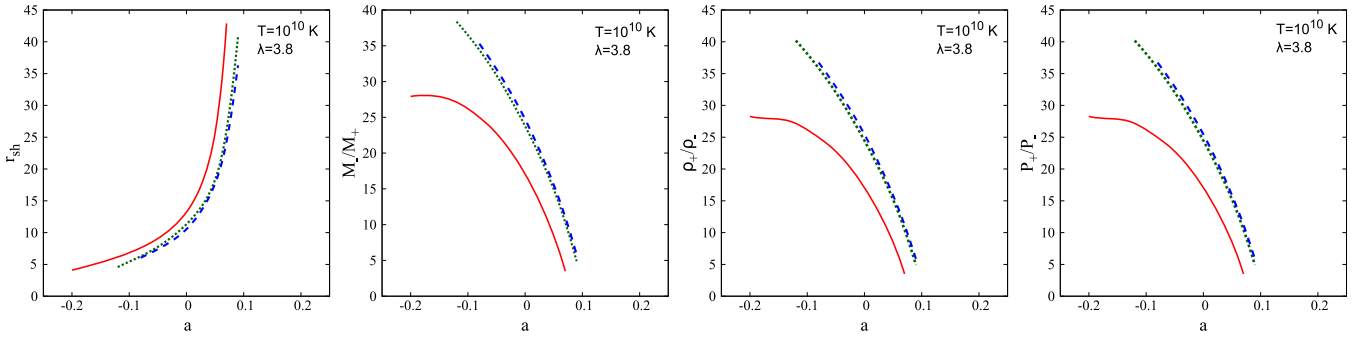


FIG. 11. Shock location–(a) $r_{\rm sh}$ (in terms of $R_g$) vs $a$, Ratios at shock–(b) $M_-/M_+$ vs $a$, (c) $\rho_+/\rho_-$ vs $a$ and (d) $P_+/P_-$ vs $a$. "−" and "+" refer to "before" and "after" shock respectively. ALP shown by red solid lines, RH shown by green dotted lines and NT shown by blue dashed lines.

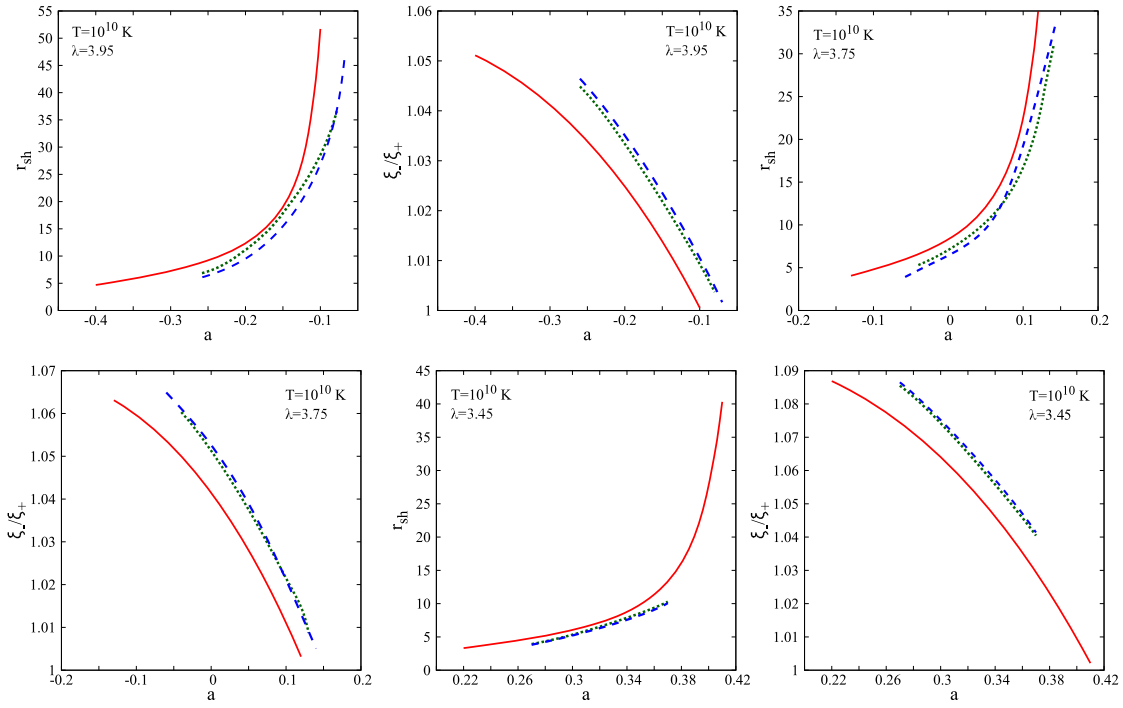


FIG. 12. Energy dissipation at shock–$\xi_-/\xi_+$ vs $a$ along with the corresponding $r_{\rm sh}$ (in terms of $R_g$) vs $a$ for $T = 10^{10}$ K and (a) $\lambda = 3.95$, (b) $\lambda = 3.75$ and (c) $\lambda = 3.45$. "-" and "+" represent quantities "before" and "after" shock respectively. ALP shown by red solid lines, RH shown by green dotted lines and NT shown by blue dashed lines.

accretion flow has larger values of the radial advective velocity. This velocity is directed, and gets randomized at the shock. The larger the value of the directed bulk velocity, the higher the amount of energy liberated when it gets randomized through shock formation. The value of the ratio of the pre- to postshock quasi-specific energy, should thus anticorrelate with $\lambda$, as well as with $(\lambda \pm a)$.

This is exactly what we observe in the figure [see three consecutive panels (a)–(c) in Fig. 12]. We also see that the amount of energy liberated can be as large as (approximately) 9%. Thus the disc may become considerably luminous (on the corresponding wavelength) at the shock, and can also produce a radiatively efficient postshock flow, at least at the shock location. It has been found (see the figures) that among the three different disc-height recipes, the NT-type of disc liberates maximum amount of energy, and hence becomes maximally luminous at the shock, provided the initial set of boundary conditions remain the same.

It also requires to be mentioned that the aforementioned energy-liberation process is not similar to the Blandford-Znajek (BZ) mechanism [108], where the rotational energy of the black hole is extracted to power jets. BZ mechanism requires the presence of poloidal magnetic field lines around a spinning black hole, which extracts the rotational energy of the hole itself. On the contrary, our simple theoretical model of purely general relativistic hydrodynamic flow does not include any magnetic energy component. The energy-liberation mechanism discussed in our work is not similar to the Penrose process [109] either, since in our model energy gets liberated at the shock location residing well outside the ergosphere.

## V. CONCLUDING REMARKS

Among various proposals to describe the geometrical configuration of matter accreting onto astrophysical black holes, flow in hydrostatic equilibrium along the vertical direction has been playing a crucial role in the study of accreting black hole systems. The local thickness of such flow configurations have been characterized using various height functions proposed in the literature over a time span of the last fifty years or so since the first-ever comprehensive work on this topic was accomplished by Novikov & Thorne [77]. The present work demonstrates that various properties of general relativistic black hole accretion, as observed in the close proximity of the hole itself, are significantly influenced by such aforementioned height functions. Our work also identifies the specific height function for which the maximally energetic flares from our Galactic Center may be determined. Properties of general relativistic postshock flows close to the astrophysical black holes have never been studied in such a comprehensive manner in the literature, as we believe.

Among the different height functions considered in the present work, the expressions of $H(r)$ as proposed by

Novikov & Thorne (NT) [77] and Riffert & Herold (RH) [78] possess a certain *truncation radius* ($r_T$), which is a function [Eq. (5)] of black hole spin angular momentum, i.e., the Kerr parameter. The presence of the truncation radius does not mean that the flow itself is disconnected from the horizon. The matter does accrete up to the horizon and plunges through it. Theoretical models of the flow thickness such as NT and RH, however, do not exist beyond $r_T$. For any $r < r_T$, the height function cannot be defined in these two cases. It is to be understood that this is a limitation of the disc models. Infalling matter does flow through the horizon–the only thing is that for all $r_+ \leq r < r_T$, the axisymmetric disc structure remains undefined. The flow joins the horizon to infinity (i.e., with the source of accreting matter like the donor, as an example, for wind driven accretion) smoothly, except at shock location where values of the flow variable change discontinuously (flow does not exhibit formation of any physical "gap"). Since the expressions for flow thickness remain undefined beyond $r_T$ for NT and RH height prescriptions, we cannot obtain the integral flow solutions for $r < r_T$. Although black hole shadow imaging involves integration of photon geodesics over the entire domain of space-time containing accreting matter, this might impose limitations while determining the exact boundary of the event horizon shadow using our flow model when characterized by the presence of $r_T$ (the Abramowicz-Lanza-Percival or ALP [79] model does not impose such limitations). This is due to the fact that the shadow of the horizon can be realized as a dark disc upon a background illuminated by photons emitted from the accreting matter. Sharpness of the peripheral boundary of such shadow will be enhanced as one can track the integral solutions closer and closer to the horizon. The nearer we will be able to get our integral stationary flow solutions to the horizon, the sharper will be the distinction between bounding lines of the shadow and the illuminated background. Hence, for accretion characterized by NT and RH discs, although overall features of the shadow will remain unchanged, the theoretically acquired distinctive sharpness of the shadow boundary will be determined by the truncation radius.

## ACKNOWLEDGMENTS

P. T. would like to acknowledge the kind hospitality provided by Harish-Chandra Research Institute, HBNI, Department of Atomic Energy, Government of India, for funding his visit through the XII[th] plan budget of Cosmology and High Energy Astrophysics Grant. The authors thank the anonymous reviewer for a meticulous scrutiny, thoughtful comments and useful suggestions which helped to improve the manuscript.

[1] A. F. Illarionov and R. A. Sunyaev, Astron. Astrophys. **39**, 185 (1975).
[2] E. P. T. Liang and P. L. Nolan, Space Sci. Rev. **38**, 353 (1984).
[3] D. V. Bisikalo, A. A. Boyarchuk, V. M. Chechetkin, O. A. Kuznetsov, and D. Molteni, Mon. Not. R. Astron. Soc. **300**, 39 (1998).
[4] A. F. Illarionov, Sov. Astron. **31**, 618 (1987).
[5] L. C. Ho, *Observational Evidence for Black Holes in the Universe*, edited by S. K. Chakrabarti (Kluwer, Dordrecht, 1999), p. 153.
[6] I. V. Igumenshchev and M. A. Abramowicz, Mon. Not. R. Astron. Soc. **303**, 309 (1999).
[7] F. Melia, Astrophys. J. **387**, L25 (1992).
[8] F. Melia, S. Liu, and R. Coker, Astrophys. J. **553**, 146 (2001).
[9] M. Moscibrodzka, T. K. Das, and B. Czerny, Mon. Not. R. Astron. Soc. **370**, 219 (2006).
[10] M. Moscibrodzka, Astron. Astrophys. **450**, 93 (2006).
[11] B. Czerny, M. Mościbrodzka, D. Proga, T. K. Das, and A. Siemiginowska, in *Proceedings of RAGtime 8/9: Workshops on Black Holes and Neutron Stars*, edited by S. Hledík and Z. Stuchlík (Silesian University in Opava, Opava, 2007), pp. 35–44.
[12] D. P. Marrone, J. M. Moran, J. H. Zhao, and R. Rao, Astrophys. J. **654**, L57 (2007).
[13] A. M. Ghez, S. Salim, N. N. Weinberg, J. R. Lu, T. Do, J. K. Dunn, K. Matthews, M. R. Morris, S. Yelda, E. E. Becklin, T. Kremenek, M. Milosavljevic, and J. Naiman, Astrophys. J. **689**, 1044 (2008).
[14] S. Gillessen, F. Eisenhauer, T. K. Fritz, H. Bartko, K. Dodds-Eden, O. Pfuhl, T. Ott, and R. Genzel, Astrophys. J. **707**, L114 (2009).
[15] K. Ferrière, Astron. Astrophys. **505**, 1183 (2009).
[16] R. Genzel, F. Eisenhauer, and S. Gillessen, Rev. Mod. Phys. **82**, 3121 (2010).
[17] T. Okuda and D. Molteni, Mon. Not. R. Astron. Soc. **425**, 2413 (2012).
[18] M. A. Abramowicz and W. H. Zurek, Astrophys. J. **246**, 314 (1981).
[19] B. Muchotrzeb and B. Paczynski, Acta Astron. **32**, 1 (1982).
[20] J. Fukue, Publ. Astron. Soc. Jpn. **35**, 355 (1983).
[21] J. F. Lu, Astron. Astrophys. **148**, 176 (1985).
[22] B. Muchotrzeb-Czerny, Acta Astron. **36**, 1 (1986).
[23] O. Blaes, Mon. Not. R. Astron. Soc. **227**, 975 (1987).
[24] S. K. Chakrabarti, Astrophys. J. **347**, 365 (1989).
[25] K. Nakayama and J. Fukue, Publ. Astron. Soc. Jpn. **41**, 271 (1989).
[26] M. A. Abramowicz and S. Kato, Astrophys. J. **336**, 304 (1989).

[27] M. A. Abramowicz and S. K. Chakrabarti, Astrophys. J. **350**, 281 (1990).
[28] H. Sponholz and D. Molteni, Mon. Not. R. Astron. Soc. **271**, 233 (1994).
[29] H. J. Bussemaker, D. Thirumalai, and J. K. Bhattacharjee, Phys. Rev. Lett. **79**, 3530 (1997).
[30] G. Tóth, R. Keppens, and M. A. Botchev, Astron. Astrophys. **332**, 1159 (1998).
[31] S. K. Chakrabarti and S. Das, Mon. Not. R. Astron. Soc. **327**, 808 (2001).
[32] T. K. Das, Astrophys. J. **577**, 880 (2002).
[33] T. K. Das, J. K. Pendharkar, and S. Mitra, Astrophys. J. **592**, 1078 (2003).
[34] T. Okuda, V. Teresi, E. Toscano, and D. Molteni, Publ. Astron. Soc. Jpn. **56**, 547 (2004).
[35] J. Fukue, Publ. Astron. Soc. Jpn. **56**, 959 (2004).
[36] J. Fukue, Publ. Astron. Soc. Jpn. **56**, 681 (2004).
[37] T. K. Das and B. Czerny, Mon. Not. R. Astron. Soc. **421**, L24 (2012).
[38] S. Saha, S. Sen, S. Nag, S. Raychowdhury, and T. K. Das, New Astron. **43**, 10 (2016).
[39] S. Majumder, S. Nag, and T. K. Das, Mon. Not. R. Astron. Soc. **480**, 3017 (2018).
[40] I. K. Dihingia, S. Das, D. Maity, and S. Chakrabarti, Phys. Rev. D **98**, 083004 (2018).
[41] J. F. Lu, Gen. Relativ. Gravit. **18**, 45L (1986).
[42] M. Kafatos and R. X. Yang, Mon. Not. R. Astron. Soc. **268**, 925 (1994).
[43] R. X. Yang and M. Kafatos, Astron. Astrophys. **295**, 238 (1995).
[44] V. I. Pariev, Mon. Not. R. Astron. Soc. **283**, 1264 (1996).
[45] K. Nakayama, Mon. Not. R. Astron. Soc. **281**, 226 (1996).
[46] S. K. Chakrabarti, Mon. Not. R. Astron. Soc. **283**, 325 (1996).
[47] S. K. Chakrabarti, Astrophys. J. **471**, 237 (1996).
[48] J. Peitz and S. Appl, Mon. Not. R. Astron. Soc. **286**, 681 (1997).
[49] K. Fukumara and S. Tsuruta, Astrophys. J. **611**, 964 (2004).
[50] P. Barai, T. K. Das, and P. J. Wiita, Astrophys. J. Lett. **613**, L49 (2004).
[51] H. Nagakura and S. Yamada, Astrophys. J. **689**, 391 (2008).
[52] H. Nagakura and S. Yamada, Astrophys. J. **696**, 2026 (2009).
[53] T. K. Das and B. Czerny, New Astron. **17**, 254 (2012).
[54] T. K. Das, S. Nag, S. Hegde, S. Bhattacharya, I. Maity, B. Czerny, P. Barai, P. J. Wiita, V. Karas, and T. Naskar, New Astron. **37**, 81 (2015).
[55] P. Suková and A. Janiuk, Mon. Not. R. Astron. Soc. **447**, 1565 (2015).
[56] P. Suková, S. Charzyński, and A. Janiuk, Mon. Not. R. Astron. Soc. **472**, 4327 (2017).
[57] P. Suková, in *RAGtime 17-19: Workshops on Black Holes and Neutron Stars*, edited by Z. Stuchlík, G. Török, and V. Karas (Silesian University in Opava, Opava, 2017), pp. 163–176.
[58] P. Tarafdar and T. K. Das, New Astron. **62**, 1 (2018).
[59] P. Tarafdar, D. A. Bollimpalli, S. Nag, and T. K. Das, Phys. Rev. D **100**, 043024 (2019).
[60] I. Palit, A. Janiuk, and P. Sukova, Mon. Not. R. Astron. Soc. **487**, 755 (2019).
[61] I. K. Dihingia, S. Das, D. Maity, and A. Nandi, Mon. Not. R. Astron. Soc. **488**, 2412 (2019).
[62] I. K. Dihingia, S. Das, and A. Nandi, Mon. Not. R. Astron. Soc. **484**, 3209 (2019).
[63] J. Fukue, Mon. Not. R. Astron. Soc. **483**, 3839 (2019).
[64] J. Fukue, Publ. Astron. Soc. Jpn. **39**, 309 (1987).
[65] M. Takahashi, D. Rillet, K. Fukumura, and S. Tsuruta, Astrophys. J. **572**, 950 (2002).
[66] M. Takahashi, Astrophys. J. **570**, 264 (2002).
[67] M. Takahashi, J. Goto, K. Fukumura, D. Rilett, and S. Tsuruta, Astrophys. J. **645**, 1408 (2006).
[68] K. Fukumura, M. Takahashi, and S. Tsuruta, Astrophys. J. **657**, 415 (2007).
[69] B. Sarkar and S. Das, J. Astrophys. Astron. **39**, 3 (2018).
[70] I. K. Dihingia, D. Maity, S. Chakrabarti, and S. Das, Phys. Rev. D **102**, 023012 (2020).
[71] N. Bilić, A. Choudhary, T. K. Das, and S. Nag, Classical Quantum Gravity **31**, 035002 (2014).
[72] V. S. Beskin, Phys. Usp. **40**, 659 (1997).
[73] I. Hubeny and V. Hubeny, Astrophys. J. **505**, 558 (1998).
[74] V. S. Beskin and A. Tchekhovskoy, Astron. Astrophys. **433**, 619 (2005).
[75] S. W. Davis and I. Hubeny, Astrophys. J. Suppl. Ser. **164**, 530 (2006).
[76] V. S. Beskin, *MHD Flows in Compact Astrophysical Objects: Accretion, Winds and Jets* (Springer, New York, 2009).
[77] I. Novikov and K. S. Thorne, *Black Holes*, edited by C. De Witt and B. De Witt (Gordon and Breach, New York, 1973).
[78] H. Riffert and H. Herold, Astrophys. J. **450**, 508 (1995).
[79] M. A. Abramowicz, A. Lanza, and M. J. Percival, Astrophys. J. **479**, 179 (1997).
[80] G. D. Karssen, M. Bursa, A. Eckart, M. Valencia-S, M. Dovčiak, V. Karas, and J. Horák, Mon. Not. R. Astron. Soc. **472**, 4422 (2017).
[81] E. Mossoux and N. Grosso, Astron. Astrophys. **604**, A85 (2017).
[82] S. R. Roberts, Y. F. Jiang, D. Q. Wang, and J. P. Ostriker, Mon. Not. R. Astron. Soc. **466**, 1477 (2017).
[83] E. Mossoux, B. Finociety, J. M. Beckers, and F. H. Vincent, Astron. Astrophys. **636**, A25 (2020).
[84] D. B. Ananda, S. Bhattacharya, and T. K. Das, Gen. Relativ. Gravit. **47**, 96 (2015).
[85] D. A. Bollimpalli, S. Bhattacharya, and T. K. Das, New Astron. **51**, 153 (2017).
[86] M. A. Shaikh, I. Firdousi, and T. K. Das, Classical Quantum Gravity **34**, 155008 (2017).
[87] M. A. Shaikh and T. K. Das, Phys. Rev. D **98**, 123022 (2018).
[88] M. A. Shaikh, Classical Quantum Gravity **35**, 055002 (2018).
[89] S. Datta, M. A. Shaikh, and T. K. Das, New Astron. **63**, 65 (2018).

[90] M. A. Shaikh, S. Maity, S. Nag, and T. K. Das, New Astron. **69**, 48 (2019).
[91] S. Datta and T. K. Das, arXiv:1910.06768.
[92] S. Maity, P. Tarafdar, M. A. Shaikh, and T. K. Das, arXiv:2005.13573.
[93] R. H. Boyer and R. W. Lindquist, J. Math. Phys. (N.Y.) **8**, 265 (1967).
[94] C. F. Gammie and R. Popham, Astrophys. J. **498**, 313 (1998).
[95] We refer [94] for the detailed description of expressions of various velocities in different frames for rotating accretion flow in the Kerr metric.
[96] R. Matsumoto, S. Kato, J. Fukue, and A. T. Okazaki, Publ. Astron. Soc. Jpn. **36**, 71 (1984).
[97] D. W. Jordan and P. Smith, *Nonlinear Ordinary Differential Equations* (Oxford University Press Inc., New York, 1999).
[98] S. H. Strogatz, *Nonlinear Dynamics and Chaos: With Applications To Physics, Biology, Chemistry, and Engineering* (Westview Press, Boulder, CO, 2001).
[99] R. C. Hilborn, *Chaos and Nonlinear Dynamics: An Introduction for Scientists and Engineers* (Oxford University Press, Oxford, 2001).
[100] K. S. Thorne, Astrophys. J. **191**, 507 (1974).
[101] C. Eckart, Phys. Rev. **58**, 919 (1940).
[102] A. H. Taub, Phys. Rev. **74**, 328 (1948).
[103] A. Lichnerowicz, *Relativistic Hydrodynamics and Magnetohydrodynamics: Lectures on the Existence of Solutions* (Benjamin, New York, 1967).
[104] K. S. Thorne, Astrophys. J. **179**, 897 (1973).
[105] A. H. Taub, Annu. Rev. Fluid Mech. **10**, 301 (1978).
[106] S. Hacyan, Gen. Relativ. Gravit. **14**, 399 (1982).
[107] H. Abraham, N. Bilić, and T. K. Das, Classical Quantum Gravity **23**, 2371 (2006).
[108] R. D. Blandford and R. L. Znajek, Mon. Not. R. Astron. Soc. **179**, 433 (1977).
[109] R. Penrose and R. M. Floyd, Nat. Phys. Sci. **229**, 177 (1971).